Journal of Hydrology 615 (2022) 128710

Contents lists available at ScienceDirect

Journal of Hydrology

journal homepage: www.elsevier.com/locate/jhydrol

Review papers

Accelerated hydrological cycle on the Tibetan Plateau evidenced by ensemble modeling of Long-term water budgets

Yibing Wang [a,b], Xianhong Xie [a,c,*], Jiancheng Shi [d], Bowen Zhu [e], Fuxiao Jiang [a,c], Yuchao Chen [a,c], Yao Liu [a,c]

[a] State Key Laboratory of Remote Sensing Science, Beijing Normal University, Beijing 100875, China
[b] Key Laboratory of Environmental Change and Natural Disaster, Beijing Normal University, Beijing 100875, China
[c] Beijing Engineering Research Center for Global Land Remote Sensing Products, Institute of Remote Sensing Science and Engineering, Faculty of Geographical Science, Beijing Normal University, Beijing 100875, China
[d] National Space Science Center, Chinese Academy of Sciences, Beijing 100190, China
[e] College of Water Science and Engineering, Taiyuan University of Technology, Taiyuan 030024, China

ARTICLE INFO

This manuscript was handled by Emmanouil Anagnostou, Editor-in-Chief, with the assistance of Jesús Mateo-Lázaro, Associate Editor

Keywords:
Tibetan Plateau
Water budget
Glacier melting
Hydrological ensemble modeling
VIC-Glacier model

ABSTRACT

Global warming potentially increases precipitation and intensifies water exchange, thereby accelerating the hydrological cycle. The Tibetan Plateau (TP) is an Asian water tower in which the water budget varies and its anomaly exerts stress on resource availability. Few studies have quantified long-term water budgets across TP owing to scarcity of ground-based observations and uncertainties in remote sensing data. In this study, water budget components (i.e., precipitation, glacial melting [GM], evapotranspiration [ET], runoff, and soil moisture [SM] state) in TP are synthetically estimated for the past three decades. The water budget estimation benefits from a GM-coupled hydrological ensemble modeling, which is forced by nine precipitation products with seven from satellite methods. The results show that the ensemble modeling effectively captures the dynamics of runoff, ET, and terrestrial water storage. The long-term average annual water input (sum of precipitation and GM) was approximately 438 mm, with ~4 % contribution from GM, for which the annual ET and runoff take away was approximately 263 and 173 mm, respectively. From 1984 to 2015, the four water fluxes significantly increased with varying rates (2.3 mm/yr, precipitation; 0.9 mm/yr, GM; 1.5 mm/yr, ET; 1.1 mm/yr, runoff), which suggested an accelerating hydrological cycle. Particularly, increasing GM (~5.8 mm/yr) in the Nyainqentanglha Mountains in southern TP induced high-yield runoff (>800 mm). These estimations aid in yielding robust solutions for water management in TP and neighboring regions. The accelerated hydrological cycle implies potential flooding risk and vulnerability of the hydrological system under climate change.

1. Introduction

The Tibetan Plateau (TP) is known as the "Third Pole," with an average altitude of over 4000 m. It is the source area of about ten major rivers, including the Yellow, Yangtze, Mekong, Salween, Brahmaputra, and Indus rivers. Runoff generated from TP provides valuable water resources for downstream regions. Precipitation and evapotranspiration (ET) dominate the land surface hydrological processes and connect processes in the hydrosphere, atmosphere, and biosphere on TP and surrounding areas (Zhang and Yang, 2010). Soil moisture (SM) acts as a distinct hydroclimatic factor characterizing land–atmosphere water and energy interchanges (Long et al., 2019; Yang et al., 2021).

In recent decades, global climate has been experiencing significant alterations owing to the natural and anthropogenic forcing (Troch et al., 2008). Climate change likely promotes increased precipitation and a higher frequency of extreme precipitation events (Silva et al., 2017), which is the main driver of ET and soil moisture dynamics. Consequently, regional and global terrestrial hydrological processes may experience various accelerations (Allan and Zveryaev, 2011; Ji et al., 2020; Liu and Curry, 2010). The acceleration of the hydrological cycle is also probably reflected in TP as the region has complex climatic conditions and extensive cryospheric landforms (Ji et al., 2020; Xu et al., 2008; Yang et al., 2011). Specifically, climate change has strengthened precipitation over the central TP, but has led to less water vapor

* Corresponding author at: State Key Laboratory of Remote Sensing Science, Beijing Normal University, Beijing 100875, China.
E-mail address: xianhong@bnu.edu.cn (X. Xie).

https://doi.org/10.1016/j.jhydrol.2022.128710
Received 6 April 2022; Received in revised form 13 September 2022; Accepted 16 October 2022
Available online 8 November 2022

exchange in the southern and eastern regions (Yang et al., 2014). Glacier melting (GM) has also been enhanced due to the disappearance of fresh snow and a decline in albedo in a warming climate (Barnett et al., 2005), thereby increasing the water supply to downstream regions (Immerzeel et al., 2010). However, the intensified hydrological cycle on TP is unstable as the precipitation and GM changes may cause substantial variability to the water partition among ET, runoff, and soil moisture (SM) (Xie et al., 2006). Meanwhile, the water budget and its dynamics are strongly coupled with energy and biological cycles (Rodriguez-Iturbe, 2000). Therefore, estimating long-term water budget components on TP is one of the most important issues under climate change and associated water resource management (Scott and Biederman, 2019).

Most studies concerning the hydrological cycle on TP illustrated only a subset of water budget components. As the main water input, precipitation shows high spatial heterogeneity because of the complex monsoons and mountain blockages on TP. It exhibited an increasing trend on TP during the past two decades (Ouyang et al., 2017; Wang et al., 2020; Zhu et al., 2011). Other than that, glacier mass change, as a unique hydrological process on TP, provides substantial water to most watersheds on TP (e.g., the sources of Salween, Brahmaputra rivers). It can be the main contributor to the increasing runoff and related hydrological factors (Lutz et al., 2014; Zhang et al., 2013). Given the precipitation and glacier melting conditions, runoff and ET are characterized by strong spatio-temporal variability (Goodrich et al., 2004; Li et al., 2014). However, few studies have attempted to provide a synthesized, quantitative view of long-term water budget patterns or quantified the change patterns of the hydrological cycle on TP. Lutz and Immerzeel (2013) estimated the TP water budget by integrating ground and satellite observations in a distributed hydrological model, but only for a short duration (2008–2010).

Moreover, estimating or modeling the water budget for TP is challenging owing to the scarcity of hydrometeorological observations and the extensive cryosphere. Given the sparse distribution of ground-based hydrological observations on TP, it is difficult to perform an acceptable hydrological modeling based on ground-based data alone (Maussion et al., 2014). Satellite products provide an encouraging alternative but have considerable discrepancies among different products, which may pose uncertainties in water budget analysis and hydrological modeling (Ullah et al., 2018; Wang et al., 2020). Ensemble method was proposed aiming to reduce subjectivity in hydrological modeling and to increase the level of confidence in simulations (Seiller et al., 2017). The method has been widely implemented and proved high performance worldwide, for example the application of ensemble precipitation forcing for streamflow simulations in the Pipiripau basin in Brazil (Strauch et al., 2012), and the ensemble physical parameterizations for rainfall forecasting in the Fuping and Zijingguan basins in Northern China (Tian et al., 2019). However, ensemble methods may face uncertainties from ensemble members, and most studies only consider three or four members in the ensemble method (Ma and Zhang, 2022; Strauch et al., 2012). Additionally, the glaciers faced variability from global climate change (Zhao et al., 2019), with obvious mass decrease in snow and/or glacier dominated regions (e.g., Alaska, Arctic Canada, Antarctic and Himalayas in TP) (Hugonnet et al., 2021; Yao et al., 2019). Glacier mass change can provide substantial water for runoff, and may regulate hydrological processes (Barnett et al., 2005). Thus, a long-term synthesis and quantitative assessment of the water budget is necessary on TP, and reasonable modeling methods are needed to consider uncertainties from the limited data and the impact of GM.

In this study, we aimed to quantify the water budgets (including precipitation, GM, ET, runoff, and SM of the top 1 m thickness) and identify the dynamic pattern of the hydrological cycle on TP over the past 30 years. To consider the impact of GM on TP, we coupled a glacier melting algorithm with the Variable Infiltration Capacity (VIC) land surface model (hereinafter named as VIC-Glacier). And as for the uncertainty from climate forcing, especially precipitation, we performed a hydrological ensemble modeling that is driven by nine precipitation products. The ensemble modeling of VIC-Glacier model would be evaluated regarding runoff, SM, ET, and water storage. After that, the spatial–temporal dynamics and uncertainties of the water budgets were calculated from the nine ensemble members. Our work improved understanding of water balance patterns on TP, thereby has implications for water resource management for TP and downstream regions. Moreover, our work indicates that an ensemble method can be reference for data-sparse areas, and presents the importance of snow and glacier melting in water balance for alpine mountains.

2. Study area and data

2.1. Study area

The TP region is situated in central Asia covering an area of approximately 2.5 million km^2 (Fig. 1). It has complex climatic conditions, including tropical humid, semi-humid, monsoon, and semi-arid climates. The average temperature ranges from 20 °C in the southeastern TP to approximately − 6 °C in the northwestern region. Influenced by multiple sources of water vapor and mountain blockage, its precipitation presents evident spatial variability, with an average annual value ranging from 50 to 2000 mm. Moreover, TP is characterized by extensive snow and glacier coverage, with a total glacier area of approximately 50,000 km^2 (Yao et al., 2007), especially in the Himalayas, Nyainqentanglha, and Tanggula mountains. Glaciers and precipitation promote a dense river network on TP, including headwaters of five major Asian rivers (the Yangtze, Yellow, Brahmaputra, Salween, and Mekong rivers).

The TP region can be divided into eight subregions: Hexi, Qaidam, Inner, Upper Yellow (UYE), Upper Yangtze (UYA), Upper Salween (US), Upper Mekong (UM), and Upper Brahmaputra (UB) watershed (Fig. 1). The first three subregions, Hexi, Qaidam, and Inner, are situated in the northern and western parts of TP, which have relatively low precipitation as the water vapor mainly comes from the mid-latitude westerlies. The other five are closed watersheds (UYE, UYA, US, UM, and UB) located in the eastern or southeastern parts of TP. In these watersheds, precipitation is relatively high because of the monsoons originating from the Arabian Sea, the South China Sea, and the Western Pacific. The eight subregions have varying glacier coverage, with the smallest area in the UYE (~134 km^2), and the largest in the UB (~4225 km^2) (Zhang et al., 2013).

2.2. Data availability and processing

2.2.1. Precipitation datasets

Precipitation is one of the most influential driving forces in hydrological modeling. Based on previous studies on precipitation evaluation, we selected nine precipitation products (Table 1) for hydrological modeling. The nine products are all widely used, and their performance have been proved on TP (Beck et al., 2017; Kai et al., 2014; Wang et al., 2020). Among the nine products, the CMA and CPC-Global products are gauge-based datasets, while the other seven products mainly rely on remote sensing retrieval and data fusion technologies. Notably, each precipitation product has its advantages and limitations, and it is difficult to establish a reliable bias correction method in places with scarce gauge observations, such as the western TP. Therefore, instead of bias correction for the precipitation products in this study, we adopted ensemble modeling to quantify the uncertainties of the simulated water budget components.

The spatial resolutions of the nine precipitation products were between 0.05° and 1.0° and four of the products had a resolution of 0.25° (i.e., CMA, CMORPH-BLD, PERSIANN-CDR, TMPA). To simplify the modeling, all precipitation products were downscaled or upscaled to the same resolution of 0.25°. Specifically, the products (i.e., CPC-Global, MSWEP, and GPCP-1DD) with a resolution coarser than 0.25° were subjected to bilinear interpolation, and the CHIRPS and CMFD products

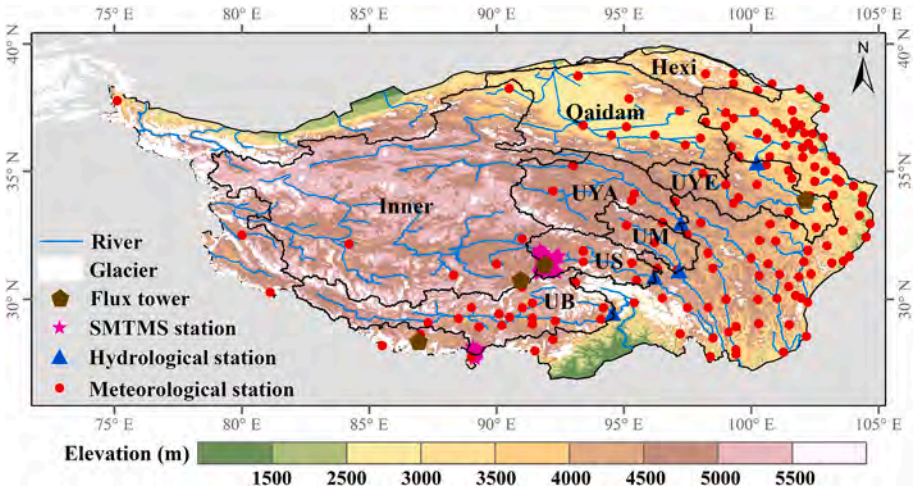

Fig. 1. Distribution of rivers and glaciers, locations of Soil Moisture and Temperature Measurement System (SMTMS) stations, streamflow stations, meteorological stations, flux towers, and boundaries of Hexi, Qaidam, Inner, Upper Yellow (UYE), Upper Yangtze (UYA), Upper Salween (US), Upper Mekong (UM), and Upper Brahmaputra (UB) subregions, with topography as the background. (For interpretation of the references to colour in this figure legend, the reader is referred to the web version of this article.)

Table 1
Overview of the nine daily precipitation products used in this study.

Precipitation product	Short name	Resolution	Period
China Meteorological Administration	CMA	0.25°	1979.1-present
Climate Prediction Center-Global	CPC-Global	0.5°	1979.1-present
Climate Hazards Group InfraRed Precipitation with Station data V2.0	CHIRPS	0.05°	1981.1-present
Multi-Source Weighted-Ensemble Precipitation V2.0	MSWEP	0.5°	1979.1-present
Climate Prediction Center MORPHing technique- gauge-satellite blended precipitation product	CMORPH-BLD	0.25°	1998.1–2018.11
Global Precipitation Climatology Project one-degree daily precipitation analysis	GPCP-1DD	1.0°	1996.10–2015.10
Precipitation Estimation from Remotely Sensed Information using Artificial Neural Networks- Climate Data Record V1R1	PERSIANN-CDR	0.25°	1983.1-present
Tropical Rainfall Measuring Mission Multi-Satellite Precipitation Analysis 3B42	TMPA	0.25°	1998.1-present
China Meteorological Forcing Dataset	CMFD	0.1°	1998.1–2018.12

Table 2
Overview of model input and verification data.

Data	Data source	Data usage
Digital Elevation Model (DEM)	U.S. Geological Survey (USGS)	River networks delineation and data interpolation
Meteorological forcing data*	China meteorological administration (CMA)	Model forcing
Vegetation data	Land cover map: Liu et al. (2010)	Model forcing
	Land cover parameters: Zhu et al. (2021)	
Soil data	Soil cover map: Zhu et al. (2020)	Model forcing
	Soil parameters: China soil dataset and Food and Agriculture Organization	
Glacier distribution data	Second Chinese Glacier Inventory	Model setup
Degree-Day Factor (DDF)	Zhang et al. (2006)	Model setup
Hydrological stations	Annual Hydrological Report for the P.R. China	Model evaluation
Eddy covariance towers	https://data.tpdc.ac.cn/zh-hans/	Model evaluation
Soil Moisture and Temperature Measurement System (SMTMS)	Su et al. (2011) and Chen et al. (2013)	Model evaluation
Global Land Evaporation Amsterdam Model (GLEAM ET)	https://www.gleam.eu/	Model evaluation
Gravity Recovery and Climate Experiment (GRACE) product	https://www2.csr.utexas.edu/grace/	Model evaluation

*The meteorological forcing data include maximum and minimum air temperature, humidity, and wind speed. The precipitation data have been described in Table 1.

with resolutions finer than 0.25° were averaged into a 0.25° resolution. Moreover, given the time span of these products and a three-year warm-up period for all hydrological simulations, the simulated water budget components were from three groups: 1984–2015 (CMA, CPC-Global, MSWEP, CHIRPS, CMFD), 1986–2015 (CMA, CPC-Global, MSWEP, CHIRPS, CMFD, PERSIANN-CDR), and 2001–2015 (CMA, CPC-Global, MSWEP, CHIRPS, CMFD, PERSIANN-CDR, CMORPH-BLD, GPCP-1DD, TMPA). The simulated water budget components during 1984–1985 period corresponded to the mean values from five simulation realizations (CMA, CPC-Global, MSWEP, CHIRPS, and CMFD); the PERSIANN-CDR-driven simulation realization was added during 1986–2001 period, and after 2001, the simulated water budget components were obtained from all the nine simulation realizations.

2.2.2. *Other model input data*

The model input data included topography, meteorological forcing, vegetation, and soil data (Table 2). The topographical data (i.e., the Digital Elevation Model [DEM]) obtained from the US Geological Survey website were used to delineate river networks and extract boundaries of subregions in TP. The meteorological forcing data included precipitation, maximum and minimum air temperatures, wind speed, and relative humidity. The precipitation has been described above, and the other forcing variables were generated by interpolating 156 CMA stations. The data from the CMA stations have undergone strict quality control to eliminate evident anomaly values (e.g., precipitation less than 0 mm) (Kai et al., 2014). The interpolation was based on the inverse distance weighting method, considering a 6.5 °C/km decline rate to reflect the temperature dependence of altitude (Xie et al., 2015).

The vegetation input includes a land-cover map for vegetation types and associated vegetation parameters. The land cover map was derived from the classification data for the year 2010 (Liu et al., 2010), and had a

spatial resolution of 1 km and 12 land cover types. Vegetation parameters were obtained from Nijssen et al. (2001) (ftp://ftp.hydro.washington.edu/). The soil input includes a soil cover map and the associated soil parameters. The soil cover map was obtained based on a 30 × 30 arc-second resolution soil characteristics dataset (Zhu et al., 2020). Soil physical parameters such as field capacity and saturated hydraulic conductivity were derived from a China soil dataset (Dai et al., 2013), and other parameters (e.g., bubbling pressure and thermal damping depth) were defined according to the soil dataset from the Food and Agriculture Organization (Nijssen et al., 2001).

The GM process simulation requires the glacier distribution and the Degree-Day Factor (DDF) parameter. The glacier distribution dataset used the second Chinese Glacier Inventory, it was generated based on remote sensing products and Google Earth images during 2004–2011 (Guo et al., 2017). The glacier distribution dataset was downloaded from the National Tibetan Plateau/Third Pole Environment Data Center (https://data.tpdc.ac.cn/zh-hans/) (Liu et al., 2012), and it has been widely used for glacier related studies (Chen et al., 2017; Su et al., 2022). The glacier distribution dataset is in vector format, and it was transferred to grids with spatial resolution of 0.005° in computation. *DDF* parameter depends on the exposure of the glacier, and is calculated based on a linear correlation between ice melt (measured by ablation stakes from different glaciers) and the sum of daily mean temperatures above the melting point (Zhang et al., 2006). The *DDFs* have been widely and successfully applied in multiple researches, including GM calculation (Lai et al., 2020; Zhao et al., 2013) and streamflow simulation (Liu et al., 2016; Zhang et al., 2013).

2.2.3. Data for model evaluation

The hydrological ensemble modeling was evaluated with observations of runoff, ET, and SM, and compared with satellite-based products of ET and Terrestrial Water Storage (TWS). Streamflow data from five stations were converted to runoff by dividing the streamflow with the associated watershed area, which was used for model calibration and validation. The streamflow data generally have long time coverage (1970 to 2010 or after), thus all nine simulation realizations can be calibrated and validated. As shown in Fig. 1, the five stations are located at the outlets of the UYE, UYA, US, UM, and UB watersheds, which are distributed in the eastern and southern parts of TP with varying degrees of glacier coverage.

The in-situ soil moisture observations were obtained from Soil Moisture and Temperature Measurement System (SMTMS) networks, containing 89 stations, with 25 stations in the Pali network and 64 stations in the Naqu network (Chen et al., 2013; Su et al., 2011). The two networks located in mid-southern TP with high altitude (>4000 m) (Fig. 1), and provided SM data of 5, 10, 20, and 40 cm depth with daily time steps for the periods from August 2010 to December 2015 and August 2015 to December 2015, respectively. It worth noting that the observed SM only referred to liquid water, so the data may have uncertainties in representing total water in frozen state (Chen et al., 2013).

ET was evaluated using observations from four eddy covariance towers and a satellite-based ET product. The eddy covariance towers are located in the southern TP, namely Naqu, Zhufeng, Namucuo, and Maqu, with forest or grass vegetation types. As a reliable remote sensing product, The Global Land Evaporation Amsterdam Model (GLEAM ET) product was used as reference data in this study, because it has been successfully applied in TP for ET evaluation and water budget calculation (Abolafia-Rosenzweig et al., 2021; Li et al., 2019). The GLEAM ET has relatively long temporal coverage (1980–present), and a spatial resolution of 0.25°.

Satellite-based TWS data were obtained from the Gravity Recovery and Climate Experiment (GRACE). This product can measure the variations in gravity and provide monthly TWS anomalies with a spatial resolution of 0.25° (Adam, 2002). GRACE has extensive applications worldwide, including water balance and TWS calculation in TP (Li et al., 2019; Liu et al., 2021; Meng et al., 2019).

3. Methods

3.1. Model description and setup

The VIC model is a land surface scheme that uses a variable infiltration curve and a nonlinear formulation to simulate the baseflow and deep soil moisture movement. The model considers multiple vegetation types and one main soil layer within each calculation unit (Liang et al., 1994; Liang et al., 1996), and it can capture the dynamics of water and energy balances. Moreover, the model calculates snow cover by dividing precipitation into rainfall and snowfall according to air temperature. Snow melt and accumulation are computed based on land surface energy balance. Thus, the VIC model has been successfully applied in studies at various scales (Cuo et al., 2013; Xie et al., 2015). In this study, we conducted the simulation with a spatial resolution of 0.25° and a temporal resolution of 3-hour.

However, the original VIC model did not consider the glacier melt process. Zhang et al. (2013) and Su et al. (2016) coupled a degree-day glacier algorithm with the VIC model (VIC-Glacier) to reflect the glacier hydrology. This study extends the application to estimate the water balance in TP. The total runoff calculated using this model is computed as follows:

$$R(i) = f \times G_i + (1-f) \times R_{vic,\,i} \tag{1}$$

where $R(i)$ is the total runoff depth (mm) in grid i, f is the glacier fraction, which is calculated by dividing the glacier area with the area of the gird cell i, $R_{vic,\,i}$ is the runoff depth (mm) in grid i calculated by the original VIC model, and G_i is the runoff from the glaciated area (mm), including liquid precipitation and glacier runoff (GM_i) in grid i. GM_i is calculated as follows:

$$GM_i = \begin{cases} DDF \times T_i; T_i > 0 \\ 0; T_i \le 0 \end{cases} \tag{2}$$

where DDF is the degree-day factor $(\mathrm{mm}/(^{\circ}\mathrm{C}{*}\mathrm{day}))$, and is determined according to Zhang et al. (2006); T_i is daily mean temperature above glacier surface (°C). A roughly estimate of T_i is assumed to be equal to the temperature of the modeling grid cell (in the size of 0.25° in the study) (Wang et al., 2021). But this may overestimate T_i, because glaciers are generally located in mountains with high attitude and low temperature. We recalculated T_i for each glacier at a finer spatial resolution (0.005°) and considered the decrease of temperature with the increase of the glacier altitude (6.5 °C per 1 km). So, T_i for GM_i calculation is lower than the grid-cell average temperature that is the forcing for other hydrological processes.

The glacier volume affects the GM estimation, and determines the upper limit of annual GM. In this study, the glacier volume was calculated using the volume-area scaling relation method (Radić et al., 2007; Radić et al., 2008):

$$V = 0.04 \times S^{1.43} \tag{3}$$

where V is the glacier volume and S is the glacier area. Considering the glacier dynamics (Ragettlia et al., 2016; Yan et al., 2021), the glacier volume and area were updated every year using equation (3). This update was repeated for all the VIC-Glacier simulation periods. Notably, snow is assumed to melt prior to the GM process, thus, the GM will be suspended if there is a snowpack on the glacier (Zhang et al., 2013). The snow calculation is consistent in non-glacier and glacier areas.

3.2. Model calibration and evaluation method

There are seven influential parameters for a VIC model simulation, namely the infiltration parameter (b_inf), three baseflow parameters (D_s, W_s, D_{smax}), and the thicknesses of three soil layers (d_1, d_2, d_3) (Liang and Xie, 2001; Zhu et al., 2020). The model was calibrated by observed

runoff from the five watersheds, and was validated regarding runoff, SM, ET and TWS. The observed runoff datasets were divided into two segments for model calibration and validation, respectively. The first segment covered approximately 20 years, and the latter one ranged between 5 and 10 years. For each simulation with one precipitation product, model calibration was conducted to adjust the seven parameters to match the simulated runoff with the observations. Each ensemble member therefore may have different model parameters according to model calibration and validation. After adjusting the parameters in the five watersheds, the adjusted parameters were transferred to ungauged regions based on their climatic similarity, i.e., similar precipitation patterns or the same climate zones (Zhu et al., 2021).

The simulated SM for the top layer will be validated with the observed SM at the depth of 10 cm from the SMTMS network. To avoid the scale difference between the simulations and the in-situ observations, the average SM values were calculated based on the multiple in-situ observations, and then they were used to validate the simulated SM of grid cells that contained the in-situ observations.

The simulated ET values were validated with four eddy covariance towers and compared with the GLEAM ET. It worth noting that the spatial resolution of the VIC-Glacier simulations is 0.25°, and each grid cell may contain a variety of vegetation types, while the eddy covariance towers can only capture small-scale ET information (<1 km). In order to relieve the mismatch of spatial scale between the two, the observed ET was used to evaluate the simulated ET with the same vegetation type in the corresponding grid.

Moreover, the simulated TWS Change (TWSC) was compared with the GRACE estimates for the period 2003–2014 at a yearly scale. The missing data in GRACE were filled by linear interpolation based on the values corresponding to the previous and following months. The yearly TWSC from GRACE was calculated as the difference between the values of December and January, and the yearly TWSC from the ensemble modeling was equal to the difference between precipitation and water output (runoff and ET). In this study, we used the Nash-Sutcliffe efficiency (NSE), correlation coefficient (R), and relative error (Er) to evaluate the performance of the nine simulation realizations.

3.3. Ensemble method and uncertainty representation

Given the nine precipitation products, we performed ensemble

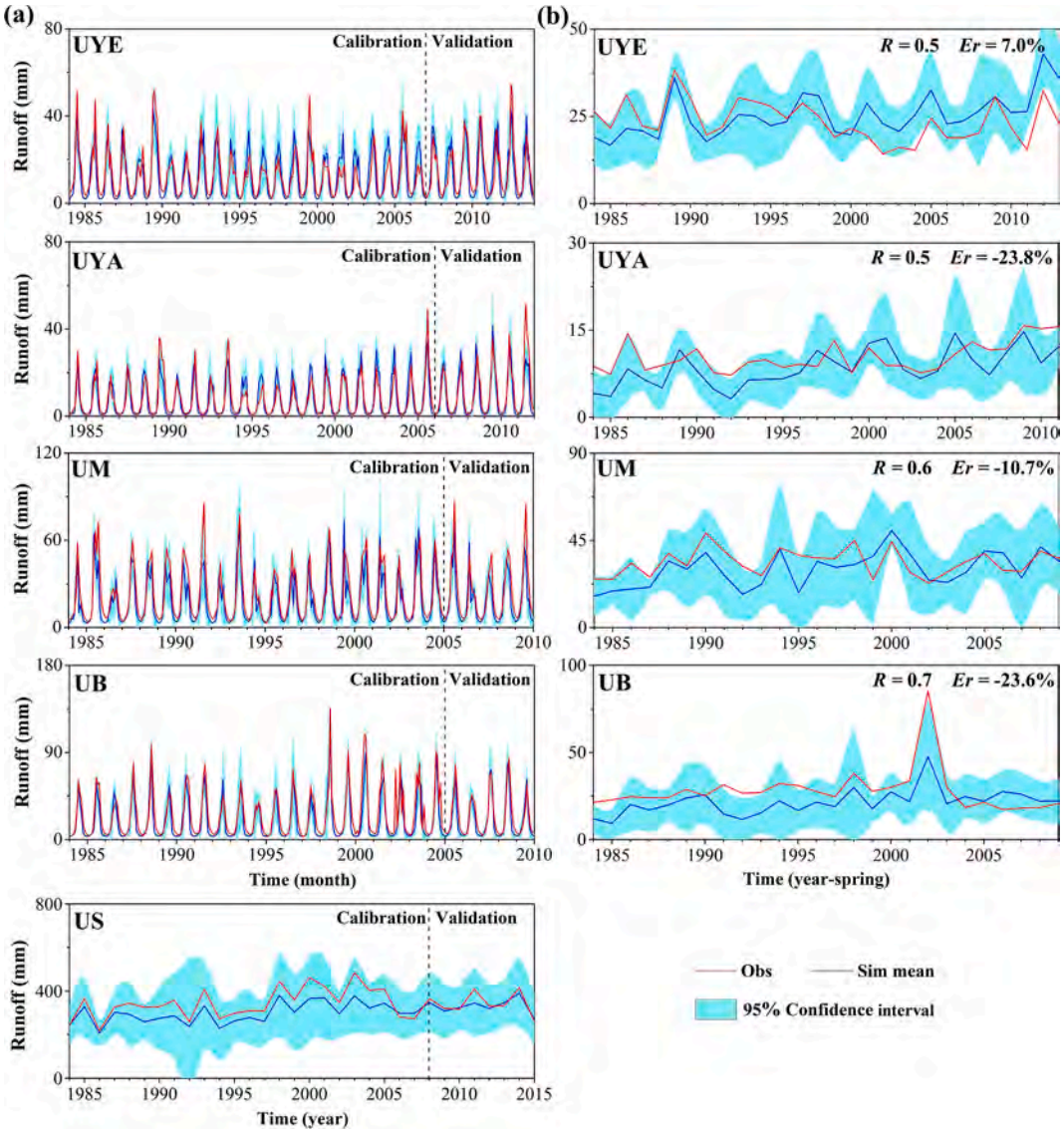

Fig. 2. Comparison of simulated monthly/annual runoff (a) and spring runoff (b) from nine simulation realizations (Sim mean) with observed runoff (Obs). The cyan areas correspond to the 95% confidence intervals of the simulation realizations. The dotted line in (a) divides the calibration and validation periods. (For interpretation of the references to colour in this figure legend, the reader is referred to the web version of this article.)

modeling with nine independent simulation realizations. The average values and 95 % confidence intervals (1.96 * standard deviation) of the nine simulation realizations were served as the values and fluctuation ranges of water budget components. Based on the knowledge of statistics and normal distribution, the average value of a dataset generally shows the highest occurrence probability, and the 95 % confidence interval can cover 95 % occurrence probability of a dataset (Anctil et al., 2009).

The uncertainty mentioned in this study refers to the discrepancy in water budget components in the nine simulation realizations, and it is usually defined by a statistical method. According to Montanari (2007), the coefficient of variation (CV) was used to measure uncertainty. Thus, the CV is calculated with respect to the uncertainty of each water budget component based on the multi-year average results of the nine simulation realizations.

4. Results

4.1. Model evaluation

The nine VIC-Glacier simulation realizations were calibrated and validated using the streamflow data from the five watersheds. As shown in Fig. 2a and Table 3, the ensemble mean based on the nine simulation realizations agreed well with the observations as they present similar dynamic changes during both the calibrated and validated periods. The mean simulation realizations achieve NSEs generally higher than 0.6 and R values over 0.8 during the calibrated period. However, the runoff simulations underestimated the observations to some degree, as the Ers were negative for the five watersheds, specifically, the Ers in the UM and UB watersheds were over −20 %. Similar patterns were showed during the validation period, the NSE and R values were approximately 0.7 and 0.9, respectively, with Ers ranging from −25 % to –3%.

Considering the absence of GM runoff observations, this study evaluated the model performance on spring runoff as the GM has a greater impact in this season (from March to May). The evaluation was conducted in UYE, UYA, UM, and UB watersheds. The US watershed was excluded as only yearly streamflow data were available there. As shown in Fig. 2b, the simulated spring runoff presented similar temporal dynamics compared to the observed data. The R values ranged between 0.5 and 0.7, and the Ers were generally negative, which indicated that the spring runoff simulations generally underestimated to some degree. However, the absolute Ers were lower than 25 % in the four watersheds, demonstrating that the VIC-Glacier model presents acceptable performance for the GM process.

Fig. 3 shows the validation results of the SM. The average SM at 10 cm obtained from the nine simulation realizations aligned with the SMTMS observations. The Er values of the Naqu and Pali networks were below 10 % and the R values were 0.88 and 0.85, respectively. The biases may be attributed to the input data, the simulation method and frozen soil. Notably, the simulations presented obvious overestimations during the winter season (from December to February in the following year). The frozen soil may be a major reason for the overestimation, as the SM observations can only represent liquid water rather than solid state, which may bring uncertainties in representing total water in winter season.

The average ET achieved by the nine simulation realizations was evaluated by ground-based observations from the four eddy covariance towers, and was compared with GLEAM ET (Fig. 4). The Er values in the Naqu and Zhufeng towers were approximately −41 % and 65 %, respectively. The large deviation may be attributed to the extensive glaciers and frozen soil cover in TP or the uncertainty within the observations. Despite the deviations, the simulated ET presented consistent daily dynamics with the observations, especially in the Maqu tower ($R > 0.8$) (Fig. 4a). In comparison with the spatial distribution and interannual variation (Fig. 4b, c), the simulated ET exhibited a similar spatial distribution and monthly dynamics as the GLEAM ET, with Er and R values of − 13.4 % and 0.98, respectively.

The simulated TWSC anomaly was further compared with the GRACE product on a yearly scale. As shown in Fig. 5, the average TWSC anomaly obtained from the nine simulation realizations were consistent with the GRACE data. The *R* values for the entire TP were approximately 0.65. The simulations present relatively poor performance in the UYE watershed with *R* of approximately 0.40, however, the *Rs* for other subregions were generally higher than 0.6, especially for the UYA and UB subregions ($R > 0.75$). Given the validation in runoff, ET, SM, and TWSC, the ensemble modeling achieves an acceptable performance for the water budget component simulation. Therefore, the simulation realizations can be used to identify the dynamics of the water balance components in TP.

4.2. Spatial-temporal variability of the long-term water budgets

The spatial distribution of the water budget components, that is, precipitation, runoff, GM, ET, SM, as well as their uncertainties, were quantified based on the nine simulation realizations. Here, SM was defined as the mean soil water content of the soil profile for the top 1 m thickness, as the SM of this thickness can characterize the seasonal cycle of soil water state without being affected by precipitation events. As shown in Fig. 6, the average annual precipitation exhibits a southeast–northwest decreasing gradient over TP. It is >1500 mm in the southern Himalayas Mountains and less than 100 mm in the northwestern part of TP. The GM is mainly distributed in mountains with high altitudes, and is approximately 16 mm. However, the GM exceeded 200 mm in the southeastern part of TP, especially in the Nyainqentanglha Mountains in Nyingchi and Changdu. Annual ET was consistent with the precipitation in terms of the spatial pattern, and ranged from below 50 mm to over 500 mm. The annual total runoff showed significant differences between the northwestern and southern TP. Specifically, it is less than 10 mm in the northwestern TP and over 800 mm in the southeastern TP. The long-term average SM ranges from 115 mm to 445 mm in TP and is represented as wet in the southeastern (>180 mm) and dry in the western part of TP (~150 mm).

The uncertainties of the five water budget components measured by the CV are shown in Fig. 7. For precipitation, the average CV was approximately 33 %, which was generally higher in the western and southern parts of TP, but it was below 20 % in the eastern TP. Large uncertainties showed in the runoff simulation, as the average CV was higher than 50 %. The CVs for ET, GM and SM were generally low (<25 %). The estimates of the five water budget components have small uncertainties in the eastern TP, but large in the southern and western regions.

The water budget components generally exhibited increasing trends during the study period (Fig. 8). Precipitation increased at a rate of 2.3 mm/yr for the entire TP, except for its decreasing trend in the southeastern Himalayas. GM increased with a value of approximately 0.9 mm/yr and exhibited the highest increase in the Nyainqentanglha Mountains. ET and runoff also exhibited increasing trends for the whole TP (~1.5 and 1.1 mm/yr), but decreasing trends in the southeastern TP. Notably, affected by precipitation and GM, runoff exhibited more complicated patterns: it generally had a decreasing trend in the

Table 3
VIC-Glacier Model performance for the five watersheds.

Watershed	Station	Calibration			Validation		
		NSE	*R*	*Er (%)*	*NSE*	*R*	*Er (%)*
UYE	**Tangnaihai**	0.69	0.85	−1.4	0.71	0.86	−4.6
UYA	**Zhimenda**	0.75	0.87	−12.3	0.71	0.87	−21.7
UM	**Changdu**	0.73	0.89	−20.3	0.69	0.89	−24.9
UB	**Nuxia**	0.67	0.91	−29.9	0.77	0.91	−20.9
US	**Jiayuqiao**	-[a]	0.92	−13.4	-[a]	0.90	−3.5

a. NSE was not calculated for this watershed because of the data availability of the yearly scale streamflow.

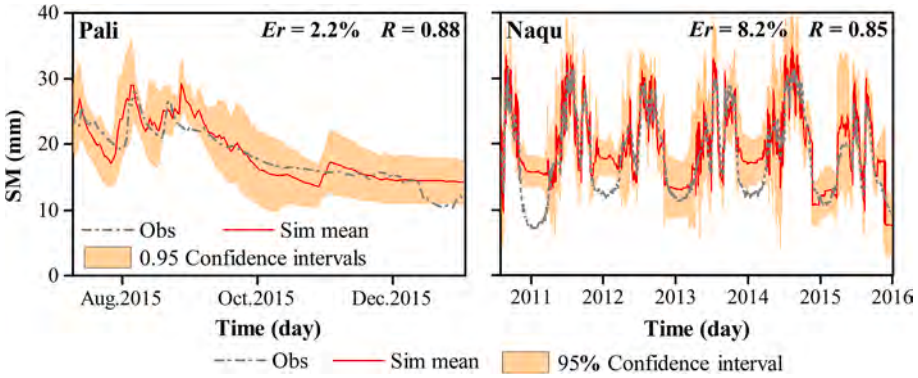

Fig. 3. Comparison of the model simulated SM with the SMTMS station data for the top 10 cm of soil thickness.

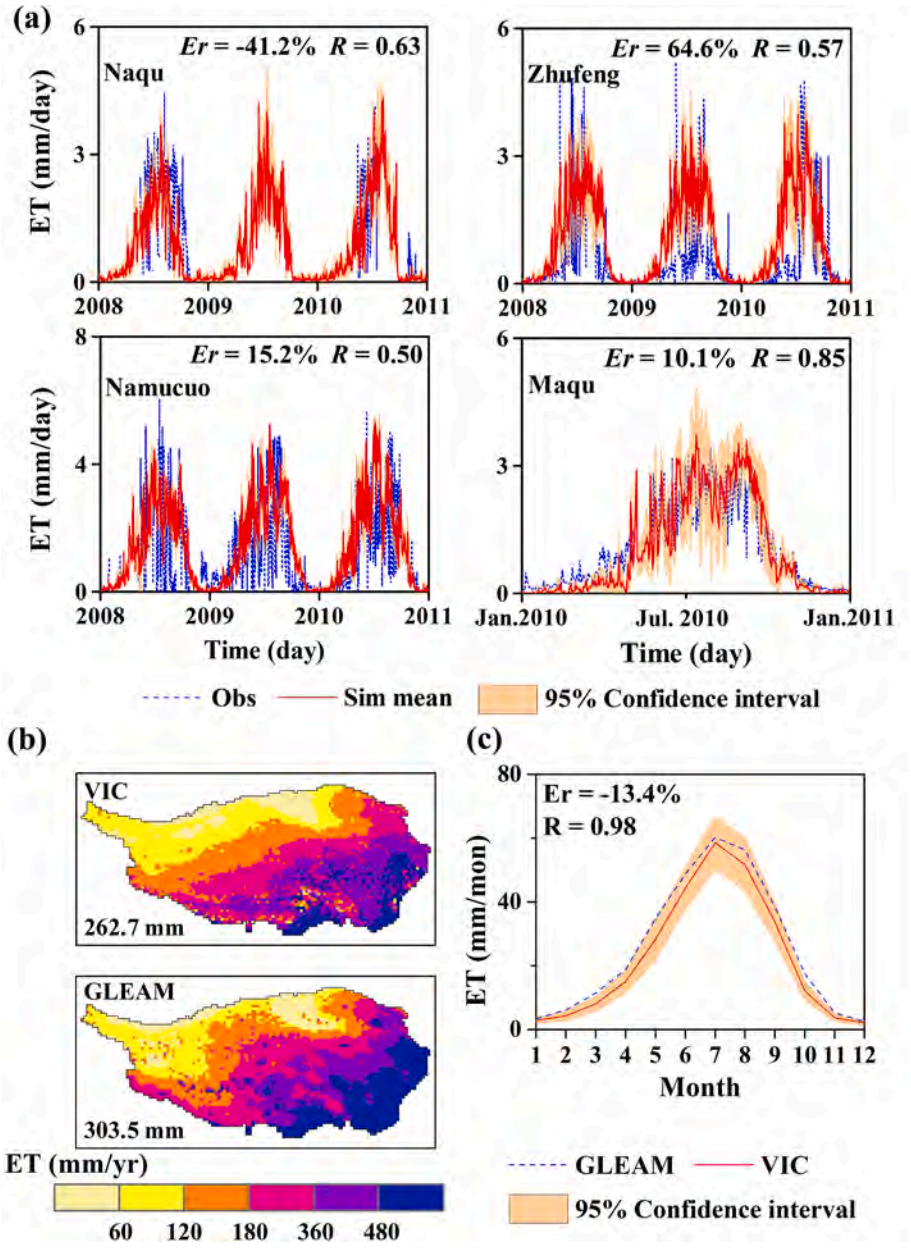

Fig. 4. Comparison of the model simulated ET with the observed data (a) and GLEAM ET (b,c).

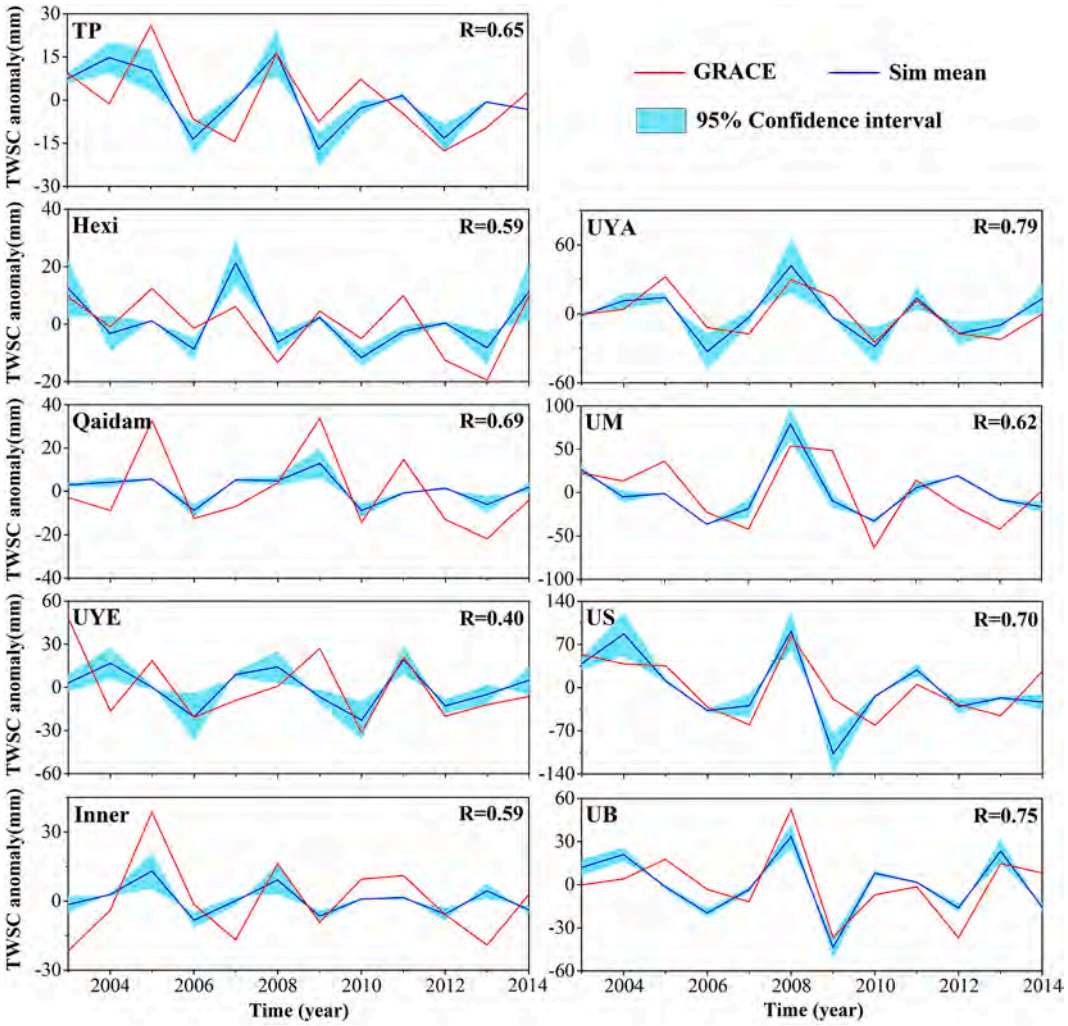

Fig. 5. Comparison of the simulated terrestrial water storage change (TWSC) with the GRACE-derived TWSC.

southeastern Himalayas, but an increasing trend in Nyainqentanglha Mountains. The SM showed slight changes during the study period (~0.1 mm/yr), and it generally increases in the western TP, and decreases in the eastern region.

4.3. Subregional-scale water budget closure

Fig. 9 shows the water budgets over TP and the eight internal subregions. We defined that the water input to the hydrological system in TP was mainly contributed by precipitation and GM. The average annual water input (sum of precipitation and GM) in TP was approximately 438 mm during the period 1984–2015, with approximately 3.7 % contribution from GM. Among the eight subregions, the annual water inputs in the Hexi, Qaidam, and Inner subregions were less than 250 mm, while the water inputs were higher than 390 mm in the other five watersheds. The largest GM contribution appeared in US (7.2 %) and Qaidam (4.4 %) subregions, but the values were less than 2 % in the UYA, UM, UYE, and Inner subregions.

As for the water output, ET accounts for a large amount of TP, with an annual value of approximately 263 mm, followed by a runoff of approximately 173 mm. The ratio of ET to water output was generally higher in the northern TP and lower in the southern part of the region. Specifically, the ratios were>70 % in the Hexi, Qaidam, UYE, Inner, and UYA subregions, but less than 65 % in the southern watersheds of TP (i.e., the US and UB watersheds). As shown in Fig. 9, the soil water storage change (ΔS) was positive (2.4 mm) for TP during the 1984–2015 period. Among the eight subregions, the UB watershed exhibited the most obvious increase (~8.8 mm) for soil water storage, followed by the UM (1.2 mm) and UYA (0.9 mm) watersheds, while the Hexi, Qaidam, and UYE subregions presented negative ΔS, suggesting a slight decrease in soil water storage. Notably, ΔS was different from TWSC, which described in Subsection 3.3 and 4.1. Here, GM was regarded as a water input for the hydrological cycle, ΔS was therefore calculated as the difference between the water input (GM and precipitation) and water output (runoff and ET), while TWSC was equal to the difference between precipitation and water output (i.e., runoff and ET).

The annual dynamics of the water budget are shown in Fig. 10 and Table 4. TP presented an acceleration of the hydrological cycle as all four water fluxes (precipitation, runoff, GM, and ET) showed increasing trends during 1984–2015. Particularly, precipitation over TP presented a sudden increase around the year of 1997, i.e., from 391 mm in the period of 1984–1997 to 439 mm during 1998–2015. However, it exhibited a slight increase of 0.5 and 0.1 mm/yr, respectively, during these two periods. The acceleration of the hydrological cycle was also demonstrated at the subregional scale, although the four water fluxes exhibited various trends. Precipitation in the Hexi subregion has the lowest increase of about 1.8 mm/yr, while the trends exceed 2.0 mm/yr in the other subregions, with the largest in the UYA, UM, and UB watersheds (~3.0 mm/yr). GM changed in the Hexi, Inner, and UM subregions with rates varying from 0.3 to 0.5 mm/yr, and the largest glacier mass loss occurred in the US watershed with rate of 3.3 mm/yr. As to the output water fluxes, the runoff and ET showed increases in the

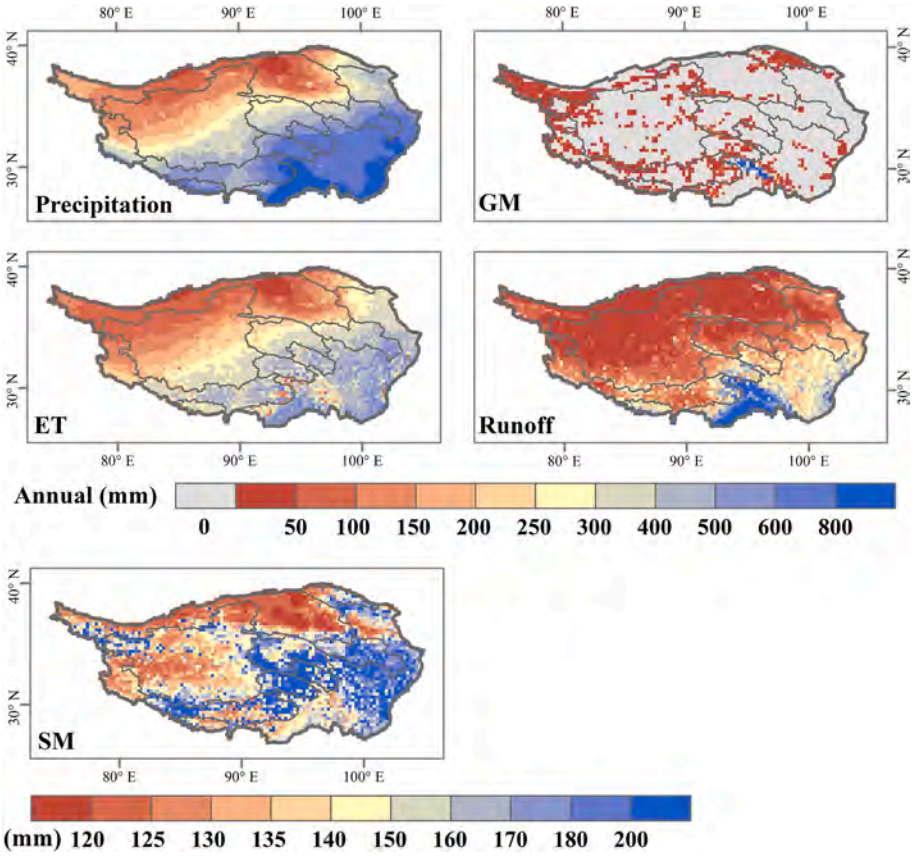

Fig. 6. Spatial distribution of annual mean precipitation, GM, ET, runoff, and SM from the ensemble modeling.

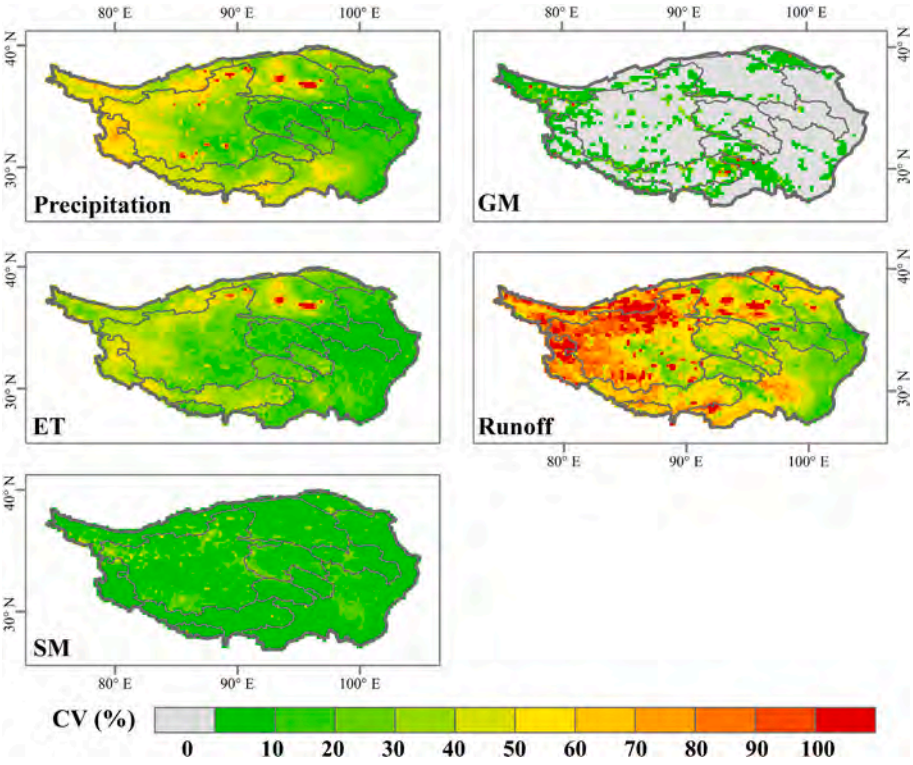

Fig. 7. Spatial distribution of coefficient of variation (CV) of precipitation, runoff, GM, ET, and SM.

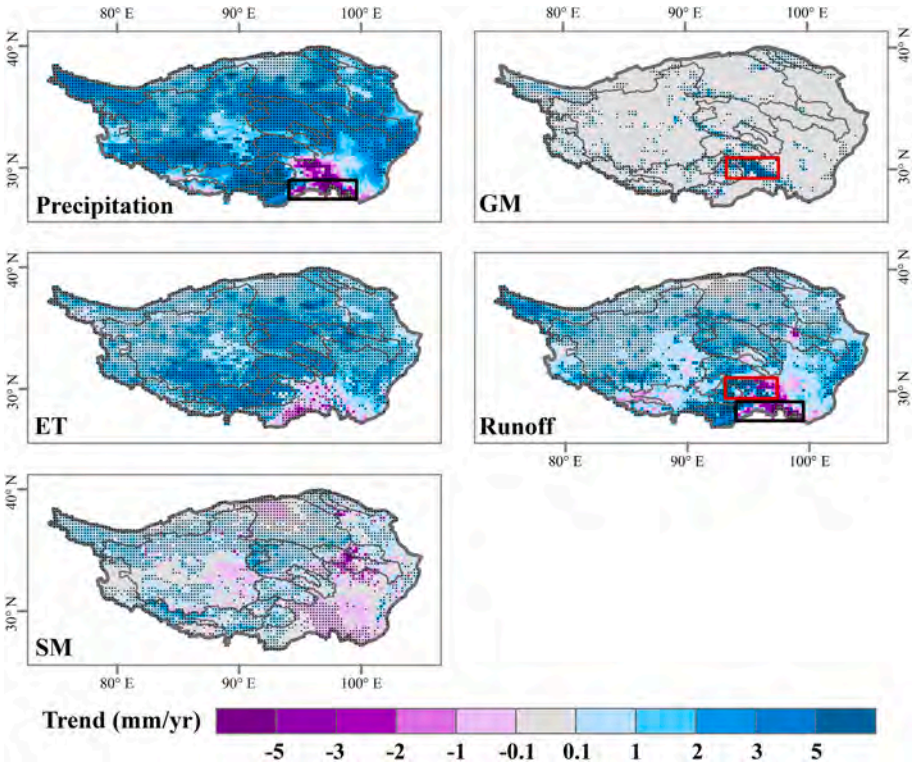

Fig. 8. Spatial distribution of annual trends of precipitation, runoff, GM, ET, and SM. The red and black rectangles represent the locations of the Nyainqentanglha Mountains and the southeastern Himalayas, respectively. The black dots indicate statistical significance (p less than 0.05). (For interpretation of the references to colour in this figure legend, the reader is referred to the web version of this article.)

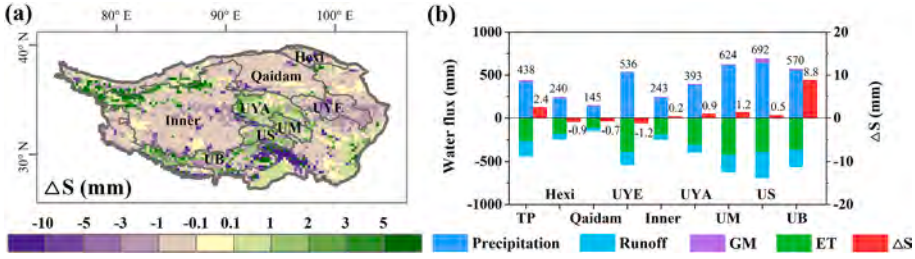

Fig. 9. Long-term average soil water storage change (ΔS) and water budgets for the period 1984–2015: (a) Spatial distribution of ΔS across TP, and (b) water budgets in TP and the eight subregions. Precipitation and GM are indicated as positive on the y-axis as they are water inputs for the hydrological system, and runoff and ET are indicated as negative because they are water outputs.

subregions located in northern and eastern TP (i.e., Hexi, Qaidam, Inner, and UYE subregions) ranging between 0.7 and 1.0 mm/yr and 1.2–2.0 mm/yr, respectively, but they have larger increases in the southern TP (i.e., US and UB subregions) with rates beyond 1.3 and 2.2 mm/yr, respectively.

The fluctuation range of each water flux varies in TP. For the entire TP, the fluctuation ranges of the average annual precipitation, GM, runoff, and ET were within 315–529, 12–20, 108–239, and 219–306 mm, respectively. The US and UB watersheds presented the largest precipitation (394–890 and 252–860 mm, respectively) and GM fluctuation ranges (42–57 and 4–23 mm, respectively). Therefore, the two watersheds generally exhibited the largest fluctuation ranges for runoff and ET. However, the UYA subregion exhibited relatively smaller fluctuation intervals of water budgets with values of ±24 mm for precipitation, ±26 mm for ET, and less than ±10 mm for GM and runoff.

4.4. Seasonal cycle of water budget components

The four water budget components (i.e., precipitation, GM, ET, and runoff) have different seasonal cycles. As shown in Fig. 11 and Table 5, for the entire TP, approximately 58 % of the precipitation occurs in summer (from June to August), with only approximately 4 % in winter (from December to February). Glaciers also experience large losses during summer (>80 %), which leads to massive water exchanges during this season (58 % of annual ET and 60 % of runoff). The eight subregions presented similar patterns in TP: precipitation and GM were prominent in summer, which promoted abundant ET and runoff (58–65 % for ET and 52–73 % for runoff). In particular, the UB watershed exhibited the highest percentage of summer precipitation (~65 %), and the US watershed had the largest summer GM (~44 mm). The seasonal cycle of SM was not shown in Fig. 11 because it was relatively stable in all four seasons (Table 5).

Regarding the water output, ET generally consumes most of the water, approximately 60 % in TP, with the highest percentage in winter (~74 %) and the lowest in autumn (~57 %), although the peak ET of approximately 60 mm per month in July. For the eight subregions, the ratios of ET to the water output ranged between 56 and 79 %, and the ratios also exhibited seasonal dynamics. The highest ratios generally

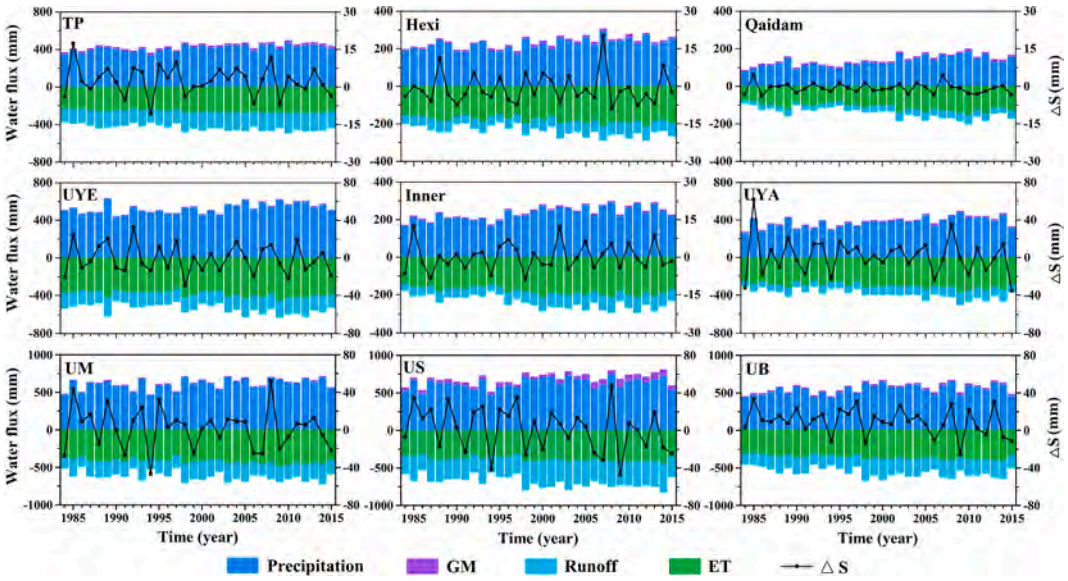

Fig. 10. Annual dynamics of water budget components in TP and the eight subregions. Precipitation and GM are indicated as positive on the y-axis as they are water inputs for the hydrological system, runoff and ET are indicated as negative because they are water outputs.

Table 4
Magnitude and the change of each water budget component in TP and the eight subregions for the period 1984–2015.

Region	Precipitation		GM		ET		Runoff		ΔS
	Mean ± std (mm)	*Trend (mm/yr)*	*Mean ± std (mm)*	*Trend* (mm/yr)*	*Mean ± std (mm)*	*Trend (mm/yr)*	*Mean ± std (mm)*	*Trend (mm/yr)*	*Mean (mm)*
TP	422.2 ± 55	2.3	16.2 ± 2	0.9	262.7 ± 22	1.5	173.2 ± 33	1.1	2.4
Hexi	231.4 ± 52	1.8	8.2 ± 1	0.3	181.0 ± 28	1.2	59.5 ± 25	0.7	−0.9
Qaidam	138.9 ± 30	2.2	6.5 ± 1	0.5	115.5 ± 20	1.7	30.7 ± 12	0.7	−0.7
UYE	535.9 ± 27	2.9	0.4 ± 0	0.7	390.0 ± 8	2.0	147.5 ± 23	1.0	−1.2
Inner	239.1 ± 31	2.5	4.1 ± 1	0.4	184.4 ± 17	1.6	58.6 ± 16	1.0	0.2
UYA	386.0 ± 24	3.4	7.0 ± 1	1.0	305.4 ± 26	2.2	86.7 ± 9	1.6	0.9
UM	621.1 ± 94	2.9	2.6 ± 1	0.4	422.0 ± 84	2.3	200.4 ± 29	0.9	1.2
US	642.2 ± 127	2.6	49.5 ± 4	3.3	390.0 ± 80	2.2	301.1 ± 59	2.6	0.5
UB	556.0 ± 155	3.1	13.6 ± 5	0.7	363.1 ± 109	2.4	197.7 ± 55	1.3	8.8

*The trend of GM is calculated for the glacier covered area of each subregion

occurred in winter, and the low values happened in summer and autumn seasons. For instance, the ratio was approximately 65 % in winter and only about 55 % in the summer and autumn seasons in the US watershed. The low percentages of summer ET implied a relatively high summer runoff generation capability. Large precipitation and GM, as well as the high conversion ratio of runoff in summer, may together cause a relatively intensive summer runoff in TP, especially in the subregions of the US and UB.

The timing of the peak runoff differed in the subregions (Fig. 11). Generally, peak flow appears in July, but it can postpone to August in the Inner and UB subregions. Intriguingly, the UYE watershed seemed to present a double peak flow regime in July and September, approximately 29 mm and 25 mm per month, respectively. The timing of peak flow is largely determined by the climatological precipitation rhythm. For example, the double peak flow regime in the UYE was consistent with the climatological pattern of precipitation.

4.5. Hotspot area with intensive runoff

The ensemble modeling showed that the changes in the water budget components have evident spatial variability. In particular, intensive precipitation and GM appeared in the southeastern TP, which caused an average runoff of>800 mm. In this area, we take two subregions, i.e., the Nyainqentanglha mountains and the southeastern Himalayas, as hotspots and identify their runoff characteristics and the contributions of precipitation and GM. The locations of the two subregions are marked in Fig. 8.

The two subregions demonstrated high runoff yield (Fig. 12), but exhibited contrasting trends during the 1984–2015 period: increased runoff in the Nyainqentanglha Mountains and decreased runoff in the southeastern Himalayas. Specifically, in the Nyainqentanglha Mountains, the average annual runoff was approximately 810 mm with an increasing rate of 5.7 mm/yr. The GM runoff contributed to over 45 % of the total runoff with a significant increase of 5.8 mm/yr. The precipitation runoff presented a decreasing change of approximately −0.1 mm/yr. In the southeastern Himalayas, however, precipitation runoff (837 mm) contributed to approximately 98 % of the total runoff (~852 mm), and it exhibited a decreasing trend (~−3.1 mm/yr), resulting in a decrease in total runoff at a rate of −2.8 mm/yr.

5. Discussion

5.1. Benefit of the ensemble modeling

The ensemble method can be established with multi-forcing modeling, multi-models and/or multi-parameter approaches, and it is inspired from modular frameworks, empirical model development, and multi-model applications (Seiller et al., 2017; Wei et al., 2020). The method benefits from extracting multiple information from the ensemble members and neutralizing the weakness of a single one,

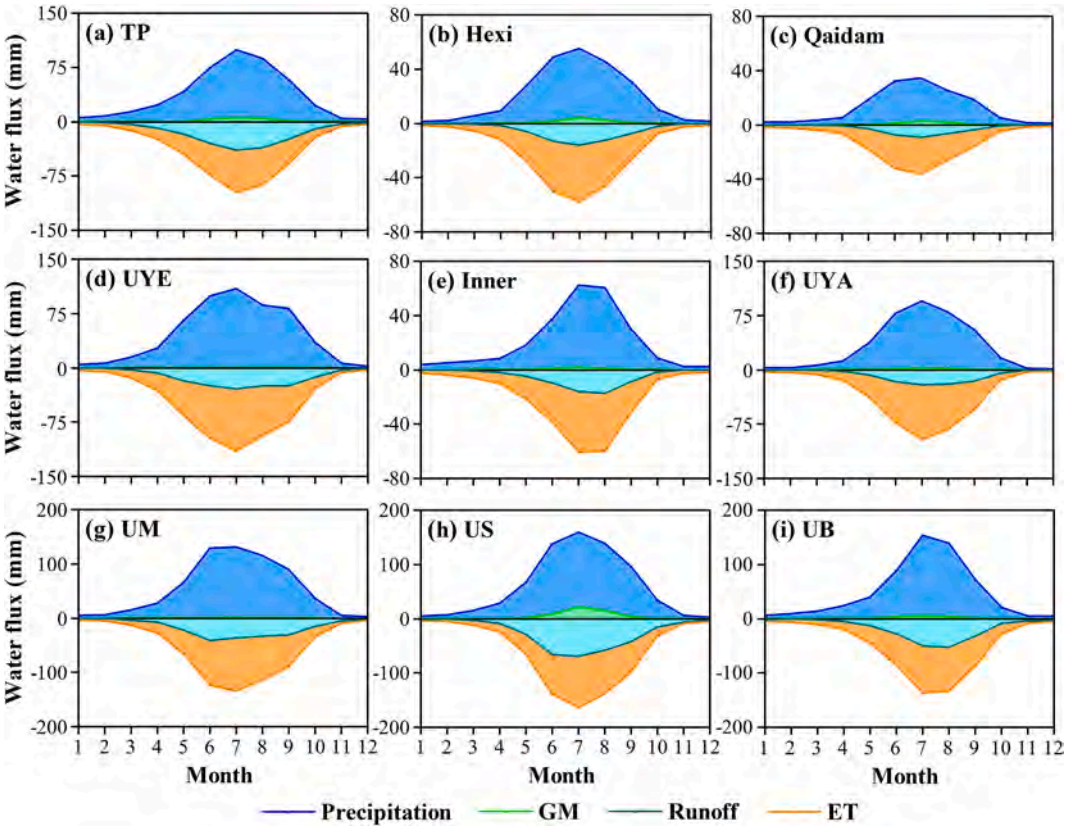

Fig. 11. Seasonal cycle of water fluxes in TP and the eight subregions during 1984–2015 period. Water fluxes include precipitation, GM, runoff, and ET, the latter two are presented as negative fluxes because they represent the water output.

thereby increasing the credibility of the simulations (Henrik et al., 2014; Strauch et al., 2012). It has been increasingly used in addressing hydrological problems, and can be a key step to mitigate uncertainties (Granata, 2019; Ma and Zhang, 2022). The ensemble method has been applied worldwide, including TP (Qi et al., 2020), Pakistan (Waseem et al., 2015), U.S. (Sharma et al., 2019), Taiwan (Yang et al., 2020), and Canada (Velázquez et al., 2009).

However, the spatiotemporal uncertainties associated with initial conditions of models and parameters may hinder the efficiency of the ensemble modelling, the method thereby is not always with acceptable performance (Velázquez et al., 2009; Yang et al., 2020). Our work selected high-performance precipitation products referring to Wang et al. (2020) before the ensemble modelling, rather than conducted the modelling directly. Moreover, our work employed more ensemble members (i.e., nine precipitation products) than most other studies thereby improving statistical significance, as more samples will likely achieve more reliable statistical estimation. The ensemble means in our work present satisfactory performance for runoff, ET, SM, and TWSC based on extensive evaluations.

Lacking of accuracy is one of the primary motivations for using an ensemble approach. Considering the insufficient data in TP, and the importance of precipitation in hydrological modelling (Strauch et al., 2012). The ensemble modelling regarding precipitation diversity may effectively improve the accuracy of water balance estimation in TP. This method is also applicable for water balance estimation in any data-sparse regions, partly because the satellite products are freely available for global scales. We further remind that the ensemble simulation strategies can be established with different situations, such as considering temperature diversity for energy balance simulation. Moreover, the ensemble modeling could provide a probabilistic assessment and uncertainties of simulations replacing the traditional method of a deterministic or single-model simulations (Velázquez et al., 2009). This study provided reliable probabilistic forecast, and confirmed the discrepancy of the nine precipitation products in TP and its influence on other water budget components.

5.2. *Estimates of long-term water budgets in TP*

Based on hydrological ensemble modeling, our study quantified the spatial patterns and seasonal cycles of the water balance components. The average annual precipitation exhibited a southeast-northwest decreasing gradient over TP, with the highest value in the southern Himalayan mountains (>1000 mm). Most of the precipitation occurred in summer (~58 %), with less than 4 % in winter. These patterns may come from multiple climatic conditions in TP as the southern region is dominated by the Indian and East Asian monsoons with high water vapor during the summer season, while the northern TP is dominated by mid-latitude westerlies with relatively low water vapor (Li et al., 2020; Zhu et al., 2011). The mean annual GM was approximately 16 mm in TP, and it exhibited significant seasonal dynamics, with over 80 % in the summer influenced by air temperature. It has been reported that the mean annual GM was about 48 mm (Wang et al., 2021), which may be an overestimation because the grid-cell average temperature was used to compute GM in equation (2). This study updated the temperature of the glacier surface by considering the elevation effect as described in subsection 3.1. Lutz et al. (2014) and Qi et al. (2022) also estimates GM in eastern TP, they showed that GM contributes approximately 16–20 % to discharge in UB watershed, which is much larger than our work. The difference likely stems from the boundary definition: the UB watershed included the Nyainqentanglha Mountains in Lutz et al. (2014) and Qi et al. (2022), but our work mainly focused on the upper watershed that excluded Nyainqentanglha Mountains. The Nyainqentanglha Mountains have extensive glacier cover and warm winds from the southern TP (Bay of Bengal, South China Sea, and the Western Pacific), resulting in a

Table 5
Annual and seasonal estimates of each water flux and state (mm) in TP and eight subregions for the period 1984–2015. The four seasons include spring (from March to May), summer (from June to August), autumn (from September to November), and winter (from December to February in the following year).

Region	Season	Precipitation	GM	ET	Runoff	SM
TP	Spring	77.6	0.9	51.0	29.9	163.2
	Summer	245.3	13.4	153.4	103.6	164.2
	Autumn	82.2	1.8	49.2	36.5	164.3
	Winter	17.1	0.0	9.2	3.2	160.5
Hexi	Spring	42.5	0.2	37.3	8.5	151.2
	Summer	140.8	7.9	111.7	41.4	151.2
	Autumn	42.8	0.1	26.2	9.5	147.6
	Winter	5.3	0.0	5.7	0.1	150.1
Qaidam	Spring	26.4	0.1	23.9	3.8	133.7
	Summer	83.0	6.2	68.9	22.4	135.1
	Autumn	24.5	0.2	17.8	4.4	132.5
	Winter	5.0	0.0	4.9	0.2	133.4
UYE	Spring	107.0	0.0	84.1	27.4	200.1
	Summer	293.0	0.4	226.7	78.1	188.4
	Autumn	122.5	0.0	69.0	40.6	182.0
	Winter	13.4	0.0	10.1	1.5	193.5
Inner	Spring	32.7	0.1	30.4	7.1	148.5
	Summer	154.4	3.9	116.0	41.1	150.1
	Autumn	40.4	0.1	29.9	10.3	152.2
	Winter	11.6	0.0	8.2	0.1	146.8
UYA	Spring	57.0	0.1	49.5	9.5	189.8
	Summer	247.1	6.6	196.6	56.2	186.5
	Autumn	74.3	0.2	51.2	20.7	185.2
	Winter	7.6	0.0	8.1	0.3	188.6
UM	Spring	107.1	0.1	72.8	33.3	210.1
	Summer	369.8	2.4	260.2	110.9	205.9
	Autumn	130.8	0.2	80.3	51.7	206.9
	Winter	13.5	0.0	8.7	4.5	208.4
US	Spring	107.8	1.5	61.1	40.2	208.6
	Summer	388.8	44.0	244.6	192.5	207.8
	Autumn	130.8	4.0	75.0	63.3	207.6
	Winter	14.7	0.0	9.3	5.1	206.8
UB	Spring	76.5	0.7	54.3	20.0	184.3
	Summer	363.4	11.6	219.7	128.9	188.1
	Autumn	95.8	1.2	78.5	44.1	193.6
	Winter	20.4	0.0	10.6	4.8	182.1

massive glacier loss (~48.2 m/yr) (Bibi et al., 2018; Yao et al., 2012). Besides that, our work demonstrated the reliable GM estimation regarding the spring runoff evaluation, and similar GM contribution values in most watersheds (e.g., US, UYA, UM, and UYE) compared with Lutz et al. (2014) and Qi et al. (2022).

Both the precipitation and GM input fluxes lead to high magnitudes of ET and runoff, especially in the summer season and the southern TP. Moreover, ET generally consumes approximately 60 % of the total water input over TP, with higher percentages in winter and the northern TP. Similar spatio-temporal pattern of ET has been observed by Yang et al. (2011) and Kuang and Jiao (2016), and also obtained by Li et al. (2019) in five source watersheds of TP, and by Zhang et al. (2018) in TP with point-scale estimation. The high ET percentage in winter may be because of the drizzle or scarce GM, which evapotranspired before being converted into runoff. The low ET percentage in the southern TP may be due to the high runoff generated from the steep mountains. We noticed Ma and Zhang (2022) used three precipitation products to drive a water-carbon coupled biophysical model, Penman-Monteith-Leuning Version 2 (PML_V2), and estimated the mean annual ET up to 353 mm for 1982–2016. This difference may result from the precipitation forcing and the modeling. Our study employed more precipitation forcing datasets to estimate water budgets in TP.

In the southeastern TP, we identified a region of high-yield runoff of over 800 mm per year. This phenomenon is mainly attributed to the high magnitudes of precipitation and GM. The monsoons and the Himalayan mountains together create a humid subtropical climate zone in the southern Himalayas, promoting annual precipitation up to 1000 mm (Gao and Liu, 2012). Additionally, the Nyainqentanglha Mountains are experiencing a warming pattern (Chen et al., 2015; Ji et al., 2020), and massive glacier loss (Bibi et al., 2018; Yao et al., 2012). Thus, the intensive GM and precipitation result in a large magnitude and an increasing trend of runoff (~5.7 mm/yr).

The uncertainties of the water budget components were calculated based on the discrepancy of the nine simulation realizations. The uncertainty of precipitation was>30 %, and generally exhibited higher values in the western and southern parts of TP. One of the primary reasons might be the different precipitation estimation instruments (e.g., infrared and microwave) (Beck et al., 2017). The high uncertainties in the western and southern parts of TP may stem from the lack of post-processing (e.g., gauge data fusion) for the products owing to the complex topography and limitations of observed data in the region (Kai et al., 2014; Wang et al., 2020). The uncertainties were transferred to the water budget estimation, the CV value for runoff was approximately 57 %, and the values for ET, GM, and SM were lower than 25 %. The high CV of runoff estimates may also be attributed to insufficient model calibration in the western TP, and the fact that runoff is more sensitive to precipitation uncertainties than the other forcing variables in general (Qi et al., 2020).

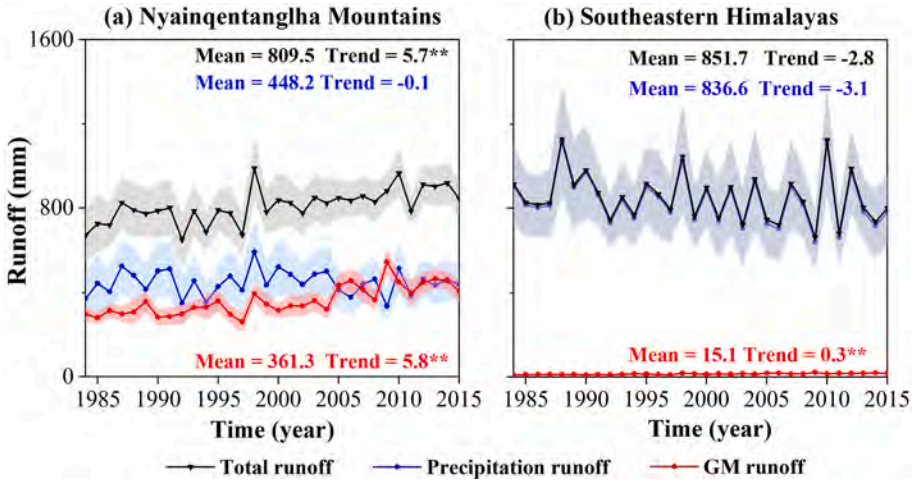

Fig. 12. Annual total runoff, GM runoff, and precipitation runoff in the two subregions: the Nyainqentanglha Mountains (a) and the southeastern Himalayas (b). The "Mean" is the long-term mean of each of the runoff in unit of mm, and the "Trend" is the linear change rate in unit of mm/yr. The double (**) and single (*) asterisks indicate significance at p less than 0.05, and p less than 0.10, respectively.

5.3. Acceleration of hydrological cycle in TP

The simulated results illustrated that TP experienced an intensified hydrological cycle during the 1980–2015 period. All the water budgets exhibit increasing trends, that is, approximately 2.3 mm/yr for precipitation, 0.9 mm/yr for GM, 1.5 mm/yr for ET, 1.1 mm/yr for runoff, and 0.1 mm/yr for SM. The increasing trends of one or several water budget components on TP have been partly evidenced in studies (Li et al., 2019; Lin et al., 2021; Lutz et al., 2014). For instance, Shi et al. (2016) found that SM increased significantly during 1980–2012, with an abrupt change in 2003. Yang et al. (2014) illustrated that precipitation, ET, runoff, and surface SM generally presented increasing trends during 1984–2006, except for the southern Himalayan Mountains. Immerzeel et al. (2012) and Wang et al. (2019) demonstrated obvious glacier loss in TP influenced by global warming. However, our work has the advantage of synthetically mapping the long-term dynamics of the water budget of TP.

The dynamic patterns may be largely attributed to the enhanced Asian summer monsoon and deep convection triggered by the thermal force. The Asian summer monsoon brings more water moisture, and deep convection exerts the troposphere stratosphere exchanges of water vapor (Fu et al., 2006). Moreover, global warming directly forces massive surface heating, thereby inducing intensive glacier loss over TP (Immerzeel et al., 2012; Sorg et al., 2012). The two result in a large amount of runoff and ET, especially in the southeastern TP (Lin et al., 2021; Xu et al., 2020). However, the southeastern Himalayas exhibit a deceleration of the hydrological cycle with decreasing precipitation, as mentioned above. This process may be attributed to the weakened water vapor exchange between the Asian monsoon region and TP with wind stilling (Yang et al., 2014).

5.4. Implications and limitations

Climate change has attracted considerable attention because of its significant impact on the hydrological and atmospheric environments (Cuo et al., 2013; Hanittinan et al., 2019). TP, which is one of the most vulnerable regions, is subject to considerable impacts of climate change on the water fluxes and states regarding precipitation, GM, ET, runoff, and SM (Immerzeel et al., 2010; Lai et al., 2020). Moreover, the water exchange in TP will exert influence on regional climate, biological, and hydrological systems in Asia, and play an important role in atmospheric circulation over Europe and North America (Duan and Duan, 2020).

The findings of this study have implications for understanding the acceleration of the hydrological cycle and its potential impacts on TP and surrounding regions under global warming. The long-term ensemble modeling illustrated that TP is undergoing increased water input, which forces higher runoff and ET, as well as a wetter condition (increasing SM) in general. ET and SM exert influence on atmospheric and biological phenomena (Peng et al., 2016; Ullah et al., 2018). For example, the increases in ET and SM may force more extensive vegetation areas, including forests and grasslands, and an overall improvement in the ecosystem and biological phenomena (Chen et al., 2015). Furthermore, runoff plays an important role in water availability, and it influences the economy and human lives regarding to floods or droughts (Immerzeel et al., 2020). Increasing runoff could promote water availability for the surrounding regions. While for the local scale of TP, the hydrological and ecological systems might tend to deteriorate. For instance, the region of the Nyainqentanglha Mountains is experiencing a large increasing trend in runoff (~5.7 mm/yr) owing to glacier mass loss (~5.8 mm/yr). The glacier area is projected to decline by>50 % at the end of the 21st century in the southern and eastern TP (Zhao et al., 2019). Therefore, runoff may introduce a high flooding risk to the TP and surrounding regions. Water resources may face a decrease in the near future (Lutz et al., 2014; Sorg et al., 2012). Thus, relevant measures such as flood prevention and water diversion should be gradually implemented and enhanced.

The uncertainty quantification for the water budget components implies the capability of the ensemble modeling method. The precipitation estimation from the ensemble products is more reliable in the eastern TP because of the small CV, and it has the largest impact on runoff simulation among the hydrological forcing variables. The hydrological ensemble modeling used in this study is capable of quantifying the uncertainties of water budgets, and estimating their fluctuation ranges (Table 4). Ensemble modeling, which extracts the benefit of available remote sensing products, could therefore provide an important reference for other studies, especially for areas with sparse ground-based observations.

This study has limitations in estimation method and model forcing data, which may introduce potential uncertainties in water budget estimation. First, the melted glacier water and the rainfall on glacier area is assumed to directly convert to surface runoff, which may cause a relative overestimation of runoff. Moreover, the degree-day glacier algorithm fails to consider glacier solidification or GM-ET conversion, probably leading to an overestimation of GM, and underestimation of ET. Second, the nine precipitation products were downscaled or upscaled for the same resolution, thus the scale change by interpolation or merging may bring additional uncertainties in precipitation and related water budget estimation. And our work only focused on uncertainties from precipitation, the other datasets for model forcing (e.g., temperature, and wind speed) merit further investigation, especially for temperature in the glacier areas. Third, the glacier volume changes were not verified due to inadequate glacier data, while we evaluated spring runoff (Fig. 2) and compared with other studies to partly reflect the glacier change. And the ground-based observations for model calibration and validation are mainly in the eastern TP, which implies the higher uncertainties of water budget estimation in the western area because of insufficient calibration. Therefore, more ground-based observations and remote sensing data are needed for model forcing and evaluation.

6. Conclusion

This study identified the hydrological cycle based on hydrological ensemble modeling of long-term water budgets (1984–2015) on TP. Ensemble modeling featured the integration of multiple precipitation products (CMA, CPC-Global, MSWEP, CHIRPS, CMFD, PERSIANN-CDR, CMORPH-BLD, GPCP-1DD, TMPA), thereby estimating the water budget components and their uncertainties. Moreover, GM and its influence were quantified using a degree-day glacier algorithm in our study. The main results are summarized as follows.

(1) The ensemble modeling method can fully utilize multiple remote sensing precipitation products and neutralize the weakness of a single forcing. It has great potential for long-term water budget estimation in areas with scarcity of ground observations.

(2) The ensemble modeling revealed that the annual water input (precipitation and GM) of TP was approximately 438 mm during the study period, with approximately 3.7 % contributed by GM. Annual ET and runoff took away approximately 263 mm and 173 mm of water, respectively; thus, the soil water storage exhibited a slightly positive change each year (~2.4 mm/yr). Furthermore, precipitation and GM exhibited various seasonal dynamics with high percentages occurring in summer, over 58 % and 83 %, respectively, which drive massive water exchanges in this season (58 % of annual ET and 60 % of runoff).

(3) The hydrological cycle exhibited an acceleration phenomenon, as evidenced by increasing precipitation (~2.3 mm/yr) and ET (~1.5 mm/yr). The hydrological cycle was more intensive in the US watershed, which exhibited larger annual water input (~642 mm) and high increasing precipitation (2.6 mm/yr) and GM (3.3 mm/yr). The southern TP presented a decreasing precipitation and runoff, but the Nyainqentanglha Mountains showed an acceleration of the hydrological cycle owing to the increasing GM.

(4) The uncertainties (the CV values) of precipitation and runoff

were >30 % and the CV of ET was approximately 25 %, followed by GM and SM. The uncertainties of the components presented a dominating spatial distribution of higher CV values in the western and southern TP. This pattern indicates that precipitation products are generally more reliable in the eastern TP than in the other parts. And the uncertainties in precipitation have the strongest influence on runoff, followed by ET.

This study has limitations regarding the modeling method and the forcing data. However, our work shows clear advantages in mapping the comprehensive water budget and identifying the acceleration of the hydrological cycle during the 1984–2015 period. The findings could provide a useful reference for ecological and environmental governance, and water management in TP and surrounding regions. Moreover, the ensemble method can be established in any other data-sparse regions, because more satellite products are freely available for global scale. To obtain more reliable water budget estimates, future studies should focus on ground-based observations of glacier dynamics, climatic and hydrological fluxes and states at a fine scale. Furthermore, uncertainties can also emerge using only one hydrological model, thus it would be beneficial to integrate more hydrological models to establish a collective and multi-data source simulation framework.

Declaration of Competing Interest

The authors declare that they have no known competing financial interests or personal relationships that could have appeared to influence the work reported in this paper.

Data availability

No data was used for the research described in the article.

Acknowledgments

This study was supported by grants from the National Natural Science Foundation of China (No. 41971030), the Strategic Priority Research Program of Chinese Academy of Sciences (Grant No. XDA20100300), and the BNU Interdisciplinary Research Foundation for the First-Year Doctoral Candidates (Grant BNUXKJC2105).

CMA stations were downloaded from http://www.nmic.cn/. CPC-Global precipitation dataset is provided by the NOAA/OAR/ESRL PSD, Boulder, Colorado, USA (https://www.esrl.noaa.gov/psd/). MSWEP precipitation dataset is developed by Hylke Beck and was downloaded from http://www.gloh2o.org/. CHIRPS precipitation dataset was downloaded from Climate Hazards Center (https://www.chc.ucsb.edu/data/chirps/). CMFD precipitation dataset was downloaded from National Tibetan Plateau Third Pole Environment Data Center (http://data.tpdc.ac.cn/en/data/8028b944-daaa-4511-8769-965612652c49/). PERSIANN-CDR precipitation dataset is developed by the Center for Hydrometeorology and Remote Sensing and were downloaded from http://chrsdata.eng.uci.edu/. CMORPH-BLD precipitation dataset was downloaded from Climate Prediction Center (https://www.cpc.ncep.noaa.gov/). GPCP-1DD precipitation dataset was downloaded from https://climatedataguide.ucar.edu/climate-data/gpcp-daily-global-precipitation-climatology-project. TMPA precipitation dataset was downloaded from Earth Sciences Data and Information SerVICes Center (GES DISC) (10.5067/TRMM/TMPA/3H/7).

References

Abolafia-Rosenzweig, R., Pan, M., Zeng, J.L., Livneh, B., 2021. Remotely sensed ensembles of the terrestrial water budget over major global river basins: an assessment of three closure techniques. Remote Sens. Environ. 252, 112191.
Adam, D., 2002. Gravity measurement: amazing grace. Nature 416 (6876), 10–11.
Allan, R.P., Zveryaev, I.I., 2011. Variability in the summer season hydrological cycle over the Atlantic-Europe region 1979–2007. Int. J. Climatol. 31 (3), 337–348.
Anctil, F., Perreault, L., Boucher, M.-A., 2009. Tools for the assessment of hydrological ensemble forecasts obtained by neural networks. J. Hydroinf. 11 (3–4), 297–307.
Barnett, T.P., Adam, J.C., Lettenmaier, D.P., 2005. Potential impacts of a warming climate on water availability in snow-dominated regions. Nature 438 (7066), 303–309.
Beck, H.E., et al., 2017. Global-scale evaluation of 22 precipitation datasets using gauge observations and hydrological modeling. Hydrol. Earth Syst. Sci. 21 (12), 6201–6217.
Bibi, S., et al., 2018. Climatic and associated cryospheric, biospheric, and hydrological changes on the Tibetan Plateau: a review. Int. J. Climatol. 38, e1–e17.
Chen, Y., et al., 2013. Evaluation of AMSR-E retrievals and GLDAS simulations against Observations of a Soil Moisture network on the central Tibetan Plateau. J. Geophys. Res. 118, 4466–4475.
Chen, X., Long, D., Hong, Y., Zeng, C., Yan, D., 2017. Improved modeling of snow and glacier melting by a progressive two-stage calibration strategy with GRACE and multisource data: how snow and glacier meltwater contributes to the runoff of the Upper Brahmaputra River basin? Water Resour. Res. 53, 1–36.
Chen, D.L., Xu, B.Q., Yao, T.D., Plateau, T., 2015. Assessment of past, present and future environmental changes on the. Chin. Sci. Bull. 60 (32), 3025–3035.
Cuo, L., Zhang, Y., Gao, Y., Hao, Z., Cairang, L., 2013. The impacts of climate change and land cover/use transition on the hydrology in the upper Yellow River Basin, China. J. Hydrol. 502, 37–52.
Dai, Y., et al., 2013. Development of a China dataset of soil hydraulic parameters using Pedotransfer functions for land surface modeling. J. Hydrometeorol. 14 (3), 869–887.
Duan, A., Duan, Q., 2020. The energy and water cycles under climate change. Natl. Sci. Rev. 7 (3), 553–557.
Fu, R., et al., 2006. Short circuit of water vapor and polluted air to the global stratosphere by convective transport over the Tibetan Plateau. Proc. Natl. Acad. Sci. 103 (15), 5664–5669.
Gao, Y.C., Liu, M., 2012. Evaluation of high-resolution satellite precipitation products using rain gauge observations over the Tibetan Plateau. Hydrol. Earth Syst. Sci. 17 (2), 837–849.
Goodrich, D.C., et al., 2004. Comparison of methods to estimate ephemeral channel recharge, alnut Gulch, San Pedro River basin Arizona. In: Hogan, J.F., Phillips, F.M., Scanlon, B.R. (Eds.), Groundwater recharge in a desert environment: The southwestern United States, Water Resources and Application Serie, 9. American Geophysical Union, Washington, DC, pp. 77–99.
Granata, F., 2019. Evapotranspiration evaluation models based on machine learning algorithms—A comparative study. Agric. Water Manag. 217, 303–315.
Guo, W., et al., 2017. The second Chinese glacier inventory: data, methods and results. J. Glaciol. 61 (226), 357–372.
Hanittinan, P., Tachikawa, Y., Ram-Indra, T., 2019. Projection of hydroclimate extreme indices over the Indochina region under climate change using a large single-model ensemble. Int. J. Climatol. 40 (6), 2924–2952.
Henrik, M., Diana, L., Marc, R., Donghua, Z., Jens Christian, R., 2014. Hydrological Ensemble Forecasting and Data Assimilation With An Integrated Hydrological Modelling System. In: 11th International Conference on Hydroinformatics, pp. 1–3.
Hugonnet, R., et al., 2021. Accelerated global glacier mass loss in the early twenty-first century. Nature 592 (7856), 726–731.
Immerzeel, W.W., et al., 2020. Importance and vulnerability of the world's water towers. Nature 577 (7790), 364–369.
Immerzeel, W.W., Van, L.P.H., Bierkens, M.F.P., 2010. Climate change will affect the Asian water towers. Science 328 (5984), 1382–1385.
Immerzeel, W.W., van Beek, L.P.H., Konz, M., Shrestha, A.B., Bierkens, M.F.P., 2012. Hydrological response to climate change in a glacierized catchment in the Himalayas. Clim. Change 110 (3), 721–736.
Ji, P., Yuan, X., Ma, F., Pan, M., 2020. Accelerated hydrological cycle over the Sanjiangyuan region induces more streamflow extremes at different global warming levels. Hydrol. Earth Syst. Sci. 24 (11), 5439–5451.
Kai, T., Su, F., Yang, D., Hao, Z., 2014. Evaluation of satellite precipitation retrievals and their potential utilities in hydrologic modeling over the Tibetan Plateau. J. Hydrol. 519, 423–437.
Kuang, X., Jiao, J.J., 2016. Review on climate change on the Tibetan Plateau during the last half century. J. Geophys. Res.: Atmos. 121, 3979–4007.
Lai, X., Xu, C.-Y., Hao, Z., Zhang, Y., 2020. Response of melt water and rainfall runoff to climate change and their roles in controlling streamflow changes of the two upstream basins over the Tibetan Plateau. Hydrol. Res. 51 (2), 272–289.
Li, X., et al., 2019. Evapotranspiration estimation for tibetan plateau headwaters using conjoint terrestrial and atmospheric water balances and multisource remote sensing. Water Resour. Res. 55, 8608–8630.
Li, D., et al., 2020. Characterizing precipitation in high altitudes of the western Tibetan plateau with a focus on major glacier areas. Int. J. Climatol. 40 (12), 5114–5127.
Li, X., Wang, L., Chen, D., Yang, K., 2014. Seasonal evapotranspiration changes (1983–2006) of four large basins on the Tibetan Plateau. J. Geophys. Res. Atmos. 119 (13), 13079–13095.
Liang, X., Lettenmaier, D.P., Wood, E.F., Burges, S.J., 1994. A simple hydrologically based model of land surface water and energy fluxes for general circulation models. J. Geogr. Res. 99 (D7), 14415–14428.
Liang, X., Wood, E.F., Lettenmaier, D.P., 1996. Surface soil moisture parameterization of the VIC-2L model: evaluation and modification. Global Planet. Change 13, 195–206.
Liang, X., Xie, Z., 2001. A new surface runoff parameterization with subgrid-scale soil heterogeneity for land surface models. Adv. Water Resour. 24, 1173–1193.
Lin, S., et al., 2021. Dynamics of evapotranspiration and variations in different land-cover regions over the Tibetan Plateau during 1961–2014. J. Hydrometeorol. 22 (4), 955–969.
Liu, J., et al., 2010. Spatial patterns and driving forces of land use change in China during the early 21st century. J. Geog. Sci. 20 (4), 483–494.

Liu, J., Curry, J.A., 2010. Accelerated warming of the Southern Ocean and its impacts on the hydrological cycle and sea ice. Proc. Natl. Acad. Sci. USA 107 (34), 14987–14992.
Liu, S., Guo, W., Xu, J., 2012. The second glacier inventory dataset of China (version 1.0) (2006-2011). In: National Tibetan Plateau Data, C. (Ed.). National Tibetan Plateau Data Center.
Liu, L., Wang, X., Niu, Q., Lun, Y., Chen, Q., 2021. Evolution characteristic of terrestrial water storage change and its attribution analysis over the Yarlung Zangbo River Basin. Trans Chin. Soc. Agric. Eng. 37 (14), 135–144.
Liu, X., Yang, T., Hsu, K., Liu, C., Sorooshian, S., 2016. Evaluating the streamflow simulation capability of PERSIANN-CDR daily rainfall products in two river basins on the Tibetan Plateau. Hydrol. Earth Syst. Sci. 21 (1), 169–181.
Long, D., et al., 2019. Generation of spatially complete and daily continuous surface soil moisture of high spatial resolution. Remote Sens. Environ. 233, 111364.
Lutz, A., Immerzeel, W., 2013. Monitoring the Tibetan Plateau Water Balance. WATGLOBS, April 2013, Beijing.
Lutz, A.F., Immerzeel, W.W., Shrestha, A.B., Bierkens, M.F.P., 2014. Consistent increase in High Asia's runoff due to increasing glacier melt and precipitation. Nat. Clim. Change 4 (7), 587–592.
Ma, N., Zhang, Y., 2022. Increasing Tibetan Plateau terrestrial evapotranspiration primarily driven by precipitation. Agric. For. Meteorol. 317, 108887.
Maussion, F., et al., 2014. Precipitation seasonality and variability over the Tibetan Plateau as resolved by the high Asia reanalysis. J. Clim. 27 (5), 1910–1927.
Meng, F., Su, F., Li, Y., Tong, K., 2019. Changes in terrestrial water storage during 2003–2014 and possible causes in Tibetan Plateau. J. Geophys. Res.: Atmos. 124 (6), 2909–2931.
Montanari, A., 2007. What do we mean by 'uncertainty'? The need for a consistent wording about uncertainty assessment in hydrology. Hydrol. Process. 21 (6), 841–845.
Nijssen, B., Schnur, R., Lettenmaier, P.D., 2001. Global retrospective estimation of soil moisture using the variable infiltration capacity land surface model, 1980–93. J. Clim. 14, 1790–1808.
Ouyang, L., Yang, K., Qin, J., Wang, Y., Lu, H., 2017. Research progress and prospect of precipitation in Himalayan region. PLATEAU METEOROLOGY 36 (5), 1165–1175.
Peng, J., Loew, A., Chen, X., Ma, Y., Su, Z., 2016. Comparison of satellite-based evapotranspiration estimates over the Tibetan Plateau. Hydrol. Earth Syst. Sci. 20 (8), 3167–3182.
Qi, W., et al., 2022. Divergent and changing importance of glaciers and snow as natural water reservoirs in the eastern and southern Tibetan Plateau. J. Geophys. Res.: Atmos. e2021JD035888.
Qi, W., Liu, J., Xia, J., Chen, D., 2020. Divergent sensitivity of surface water and energy variables to precipitation product uncertainty in the Tibetan Plateau. J. Hydrol. 581, 124338.
Radić, V., Hock, R., Oerlemans, J., 2007. Volume–area scaling vs flowline modelling in glacier volume projections. Ann. Glaciol. 46, 234–240.
Radić, V., Hock, R., Oerlemans, J., 2008. Analysis of scaling methods in deriving future volume evolutions of valley glaciers. J. Glaciol. 54, 601–612.
Ragettlia, S., Immerzeel, W.W., Pellicciottic, F., 2016. Contrasting climate change impact on river flows from high-altitude catchments in the Himalayan and Andes Mountains. Proc. Natl. Acad. Sci. USA 113 (33), 9222–9227.
Rodriguez-Iturbe, I., 2000. Ecohydrology: a hydrologic perspective of climate-soil-vegetation dynamies. Water Resour. Res. 36 (1), 3–9.
Scott, R.L., Biederman, J.A., 2019. Critical zone water balance over 13 years in a semiarid savanna. Water Resour. Res. 55 (1), 574–588.
Seiller, G., Anctil, F., Roy, R., 2017. Design and experimentation of an empirical multistructure framework for accurate, sharp and reliable hydrological ensembles. J. Hydrol. 552, 313–340.
Sharma, S., Siddique, R., Reed, S., Ahnert, P., Mejia, A., 2019. Hydrological model diversity enhances streamflow forecast skill at short- to medium-range timescales. Water Resour. Res. 55 (2), 1510–1530.
Shi, L., Du, J., Zhou, K., Zhuo, G., 2016. The temporal-spatial variations of soil moisture over the Tibetan Plateau during 1980–2012. J. Glaciol. Geocryol. 38 (5), 1241–1248.
Silva, R.O.B.d., Montenegro, S.M.G.L., Souza, W.M.d., 2017. Tendências de mudanças climáticas na precipitação pluviométrica nas bacias hidrográficas do estado de Pernambuco. Engenharia Sanitaria e Ambiental, 22(3): 579-589.
Sorg, A., Bolch, T., Stoffel, M., Solomina, O., Beniston, M., 2012. Climate change impacts on glaciers and runoff in Tien Shan (Central Asia). Nat. Clim. Change 2 (10), 725–731.
Strauch, M., et al., 2012. Using precipitation data ensemble for uncertainty analysis in SWAT streamflow simulation. J. Hydrol. 414–415, 413–424.
Su, Z., et al., 2011. The Tibetan Plateau observatory of plateau scale soil moisture and soil temperature (Tibet-Obs) for quantifying uncertainties in coarse resolution satellite and model products. Hydrol. Earth Syst. Sci. 15 (7), 2303–2316.
Su, F., et al., 2016. Hydrological response to future climate changes for the major upstream river basins in the Tibetan Plateau. Global Planet. Change 136, 82–95.
Su, B., et al., 2022. Glacier change in China over past decades: Spatiotemporal patterns and influencing factors. Earth Sci. Rev. 226, 103926.
Tian, J., Liu, J., Yan, D., Ding, L., Li, C., 2019. Ensemble flood forecasting based on a coupled atmospheric-hydrological modeling system with data assimilation. Atmos. Res. 224, 127–137.
Troch, P.A., Bierkens, M., Dolman, A.J., Troch, P.A., 2008. Global warming and the acceleration of the hydrological cycle. Clim. Hydrol. Cycle 1–12.
Ullah, W., Wang, G., Gao, Z., Hagan, D.F.T., Lou, D., 2018. Comparisons of remote sensing and reanalysis soil moisture products over the Tibetan Plateau, China. Cold Reg. Sci. Technol. 146, 110–121.
Velázquez, J.A., et al., 2009. An evaluation of the Canadian global meteorological ensemble prediction system for short-term hydrological forecasting. Hydrol. Earth Syst. Sci. 13, 2221–2231.
Wang, Y., et al., 2020. Magnitude agreement, occurrence consistency, and elevation dependency of satellite-based precipitation products over the Tibetan Plateau. Remote Sens. 12 (11), 1750.
Wang, N., Yao, T., Xu, B., Chen, A., Wang, W., 2019. Spatiotemporal pattern, trend, and influence of glacier change in Tibetan Plateau and surroundings under global warming. J. Chin. Acad. Sci. 34 (11), 1220–1232.
Wang, Y., Xie, X., Shi, J., Zhu, B., 2021. Ensemble runoff modeling driven by multi-source precipitation products over the Tibetan Plateau. Chin Sci Bull. 66 (32), 4169–4186.
Waseem, M., Ajmal, M., Kim, T.-W., 2015. Ensemble hydrological prediction of streamflow percentile at ungauged basins in Pakistan. J. Hydrol. 525, 130–137.
Wei, Z., et al., 2020. Identification of uncertainty sources in quasi-global discharge and inundation simulations using satellite-based precipitation products. J. Hydrol. 589, 125180.
Xie, X., et al., 2015. Detection and attribution of changes in hydrological cycle over the Three-North region of China: climate change versus afforestation effect. Agric. For. Meteorol. 203, 74–87.
Xie, Z.C., Wang, X., Kang, E.S., Feng, Q.H., Li, Q.Y., 2006. Glacial runoff in China: an evaluation and prediction for the future 50 years -in Chinese. J. Glaciol. Geocryol. 28 (4), 457–466.
Xu, J., Gao, Y., Peng, B., Wang, Y., 2020. Change characteristics of precipitation and its cause during 1979–2016 over the Qinghai-Tibetan Plateau. Plateau Meteorol. 39 (2), 234–244.
Xu, Z.X., Gong, T.L., Li, J.Y., 2008. Decadal trend of climate in the Tibetan Plateau—Regional temperature and precipitation. Hydrol. Process. 22 (16), 3056–3065.
Yan, X., et al., 2021. Accelerated glacier mass loss with atmospheric changes on Mt. Yulong, Southeastern Tibetan Plateau. J. Hydrol. 603, 126931.
Yang, K., et al., 2011. Response of hydrological cycle to recent climate changes in the Tibetan Plateau. Clim. Change 109 (3–4), 517–534.
Yang, K., et al., 2014. Recent climate changes over the Tibetan Plateau and their impacts on energy and water cycle: a review. Global Planet. Change 112, 79–91.
Yang, S.-C., et al., 2020. Development of a hydrological ensemble prediction system to assist with decision-making for floods during typhoons. Sustainability 12 (10), 4258.
Yang, C., Ma, Y., Yuan, Y., 2021. Terrestrial and atmospheric controls on surface energy partitioning and evaporative fraction regimes over the Tibetan Plateau in the growing season. J. Geophys. Res.: Atmos.
Yao, T., et al., 2012. Different glacier status with atmospheric circulations in Tibetan Plateau and surroundings. Nat. Clim. Change 2 (9), 663–667.
Yao, T., et al., 2019. Recent third pole's rapid warming accompanies cryospheric melt and water cycle intensification and interactions between monsoon and environment: multidisciplinary approach with observations, modeling, and analysis. Bull. Am. Meteorol. Soc. 100 (3), 423–444.
Yao, T., Pu, J., Lu, A., Wang, Y., Yu, W., 2007. Recent glacial retreat and its impact on hydrological processes on the Tibetan Plateau, China, and Surrounding Regions. Antarct. Alpine Res. 39 (4), 642–650.
Zhang, T., et al., 2018. Climate-related trends of actual evapotranspiration over the Tibetan Plateau (1961–2010). Int. J. Climatol. 38, e48–e56.
Zhang, Y., Liu, S., Ding, Y., 2006. Observed degree-day factors and their spatial variation on glaciers in western China. Ann. Glaciol. 43 (1), 301–306.
Zhang, L., Su, F., Yang, D., Hao, Z., Tong, K., 2013. Discharge regime and simulation for the upstream of major rivers over Tibetan Plateau. J. Geophys. Res. 118 (15), 8500–8518.
Zhang, X.L., Yang, M.X., 2010. Evapotranspiration in the Tibetan Plateau Based on GAME-Tibet IOP Data. Scientia Geographica Sinica 30 (6), 929–935.
Zhao, Q., et al., 2013. Coupling a glacier melt model to the Variable Infiltration Capacity (VIC) model for hydrological modeling in north-western China. Environ. Earth Sci. 68 (1), 87–101.
Zhao, Q., et al., 2019. Projecting climate change impacts on hydrological processes on the Tibetan Plateau with model calibration against the glacier inventory data and observed streamflow. J. Hydrol. 573, 60–81.
Zhu, B., et al., 2021. Extensive evaluation of a continental-scale high-resolution hydrological model using remote sensing and ground-based observations. Remote Sens. 13 (7), 1247.
Zhu, X., Bothe, O., Fraedrich, K., 2011. Summer atmospheric bridging between Europe and East Asia: Influences on drought and wetness on the Tibetan Plateau. Quat. Int. 236 (1), 151–157.
Zhu, B., Xie, X., Meng, S., Lu, C., Yao, Y., 2020. Sensitivity of soil moisture to precipitation and temperature over China: present state and future projection. Sci. Total Environ. 705, 135774.